Title: The epigenomic landscape of single vascular cells reflects developmental origin and identifies disease risk loci

Authors: Chad S. Weldy, M.D., Ph.D.[1,2,#], Soumya Kundu, Ph.D.[3,4], João Monteiro, Ph.D.[1], Wenduo Gu, Ph.D.[1], Albert J. Pedroza, M.D.[6], Alex R. Dalal, M.D.[6], Matthew D. Worssam, Ph.D.[1], Daniel Li, M.D.[1], Brian Palmisano, M.D., Ph.D.[1], Quanyi Zhao, Ph.D.[1], Disha Sharma, Ph.D.[1], Trieu Nguyen, B.S.[1], Ramendra Kundu, Ph.D.[1], Michael P. Fischbein, M.D., Ph.D.[5,6], Jesse Engreitz, Ph.D.[4], Anshul B. Kundaje, Ph.D.[3,4], Paul P. Cheng, M.D., Ph.D.[1,6], Thomas Quertermous, M.D.[1,6,#]

[1]Department of Medicine, Division of Cardiovascular Medicine, Stanford University
[2]Stanford Center for Inherited Cardiovascular Disease
[3]Department of Computer Science, Stanford University
[4]Department of Genetics, Stanford University
[5]Department of Cardiothoracic Surgery, Stanford University
[6]Stanford Cardiovascular Institute, Stanford University

Running title: Epigenomic landscape of single vascular cells

[#]Co-correspondance:
Chad S. Weldy, MD., PhD
Falk CVRC, Rm 138
300 Pasteur Drive
Stanford, CA 94305
Email: weldyc@stanford.edu

Thomas Quertermous, M.D.
Falk CVRC, Rm 265
300 Pasteur Drive
Stanford, CA 94305
Email: tomq1@stanford.edu

Short title: Epigenomic landscape of single vascular cells

One Sentence Summary: Epigenomic landscape are not only cell type, but vascular site specific, with important implications in regulating vascular site-specific disease risk.

Abstract

Vascular sites have distinct susceptibility to atherosclerosis and aneurysm, yet the biological underpinning of vascular site-specific disease risk is largely unknown. Vascular tissues have different developmental origins that may influence global chromatin accessibility, and understanding differential chromatin accessibility, gene expression profiles, and gene regulatory networks (GRN) on single cell resolution may give key insight into vascular site-specific disease risk. Here, we performed single cell chromatin accessibility (scATACseq) and gene expression profiling (scRNAseq) of healthy adult mouse vascular tissue from three vascular sites, 1) aortic root and ascending aorta, 2) brachiocephalic and carotid artery, and 3) descending thoracic aorta. Through a comprehensive analysis at single cell resolution, we discovered key regulatory enhancers to not only be cell type, but vascular site specific in vascular smooth muscle (SMC), fibroblasts, and endothelial cells. We identified epigenetic markers of embryonic origin with differential chromatin accessibility of key developmental transcription factors such as *Tbx20*, *Hand2*, *Gata4*, and *Hoxb* family members and discovered transcription factor motif accessibility to be cell type and vascular site specific. Notably, we found ascending fibroblasts to have distinct epigenomic patterns, highlighting SMAD2/3 function to suggest a differential susceptibility to TGFβ, a finding we confirmed through *in vitro* culture of primary adventitial fibroblasts. Finally, to understand how vascular site-specific enhancers may regulate human genetic risk for disease, we integrated genome wide association study (GWAS) data for ascending and descending aortic dimension, and through using a distinct base resolution deep learning model to predict variant effect on chromatin

accessibility, ChromBPNet, to predict variant effects in SMC, Fibroblasts, and Endothelial cells within ascending aorta, carotid, and descending aorta sites of origin. We reveal that although cell type remains a primary influence on variant effects, vascular site modifies cell type transcription and highlights genomic regions that are enriched for specific TF motif footprints — including MEF2A, SMAD3, and HAND2. This work supports a paradigm that the epigenomic and transcriptomic landscape of vascular cells are cell type and vascular site-specific and that site-specific enhancers govern complex genetic drivers of disease risk.

75 **Introduction**

76 The risk to develop vascular disease is vascular site-specific — a clinical
77 observation that has been well described for over a half century[1-3], yet the biological
78 mechanisms by which this occurs remain poorly understood. Smooth muscle cells
79 (SMC), fibroblasts, and endothelial cells, which make up vascular tissues, have distinct
80 developmental origins[4-10] and this embryonic lineage diversity has been hypothesized to
81 contribute to vascular site specific susceptibility to disease[5]. Genome wide association
82 studies (GWAS) of vascular disease have revealed unique loci for disease in individual
83 vascular sites, highlighting differential genetic and molecular etiologies for disease in
84 differing vascular tissues[11-17]. Understanding the fundamental mechanisms that mediate
85 this differential susceptibility to disease is critical to understand mechanisms of vascular
86 disease and discover novel therapeutic targets.

87 Genomic structure and chromatin accessibility within the cell is intricately linked
88 to function and governs transcriptional programs that drive disease risk[18]. This context
89 is important when considering that heritability of complex disease is determined by
90 common genetic variation that largely mediates disease risk through modifying genomic
91 enhancer function within regions of open chromatin[19]. The recent advancement of single
92 cell global chromatin accessibility profiling through *A*ssay for *T*ransposase *A*ccessible
93 *C*hromatin *seq*uencing (scATACseq) in combination with single cell transcriptomic
94 analysis (scRNAseq) has further defined that genetic risk of cardiac[20,21] and vascular
95 disease[22-24] is driven in part through modification of cell type specific enhancers
96 regulating expression of disease modifying genes in a cell type specific manner.

97 During vasculogenesis in early life, the carotid arteries and great vessels of the
98 heart form from the pharyngeal arch arteries which appear in a craniocaudal sequence
99 and then regress or remodel to form a definitive vascular pattern[25-28]. The adult murine
100 aorta is composed of vascular cells from diverse embryonic origin including the
101 secondary heart field, neural crest, and somitic mesoderm[5] and reside in spatially
102 distinct domains[8]. Further, analysis of smooth muscle cells from adult healthy vascular
103 tissue in mouse has shown a differential gene expression profile across vascular sites,
104 which suggests relevance to vascular site-specific disease risk[29,30].
105 Epigenomic landscape of tissues may be influenced by embryonic origin, yet cell
106 type specific enhancers of vascular tissues between vascular sites have yet to be
107 mapped. By performing scATACseq combined with scRNAseq of healthy adult mouse
108 aortic tissue from three vascular sites, 1) aortic root and ascending aorta, 2)
109 brachiocephalic and carotid artery, and 3) descending thoracic aorta — representing the
110 secondary heart field and neural crest, neural crest, and somitic mesoderm, respectively
111 — we report that cell type specific enhancers of vascular cells are vascular site specific,
112 suggest a developmental “memory”, and are related to disease risk genes. Through a
113 comprehensive approach utilizing gene regulatory networks (GRN), *in vitro* culture of
114 primary adventitial fibroblasts, and a novel technique to develop machine learning
115 neural networks (ChromBPNet) to predict human variant effect within cell types across
116 vascular sites, we not only reveal key differential chromatin accessibility of transcription
117 factor (TF) motifs between vascular sites but provide data to support the hypothesis that
118 genetic variants regulate cell function in not only a cell type, but vascular site-specific
119 mechanism. This work provides important insights into disease risk across vascular

120 tissues and supports the concept that the epigenomic landscape of vascular cells is
121 vascular site-specific and regulates disease risk.
122
123 **Results**
124 **Single cell analysis of vascular tissue reveals cell type and vascular site specific**
125 **epigenomic profiles**
126 We performed microdissections to collect the vascular tissues from three
127 vascular sites in 16 healthy adult C57Bl/6 male mice (14-16 weeks of age) including the
128 1) ascending aorta and aortic root, 2) brachiocephalic and right common carotid
129 arteries, and 3) descending thoracic aorta (**Fig 1A**). Tissues were pooled by vascular
130 site, underwent enzymatic digestion and mechanical dissociation, live cells were FACS
131 sorted, and cells were then partitioned for either scRNAseq or for subsequent nuclei
132 isolation and scATACseq using 10X genomics platform as previously described[22,31,32].
133 Following quality control and removal of low-quality cells, data was normalized and
134 underwent linear dimensional reduction following standard protocols in R packages
135 Seurat and Signac[33]. A total of 37,394 cells and 40,275 cells were of high data quality
136 and were profiled with scRNAseq and scATACseq respectively with roughly 10,000-
137 15,000 cells per vascular site and sequencing modality. Visualization with UMAP
138 methodology for both scRNAseq and scATACseq datasets was performed (**Fig 1B&C**).
139 UMAP visualization of scRNAseq and scATACseq data reveals a specific pattern where
140 vascular site origin distinguishes cell clusters (**Fig 1B&C**).
141 Given the interrelationship between RNA expression and global chromatin
142 accessibility, these datasets were then integrated together as previously described[22,33].

143 Integrated scRNAseq and scATACseq datasets underwent additional non-linear
144 dimensional reduction and UMAP visualization (**Fig 1D**). The integrated UMAP
145 representing both transcriptomic and chromatin accessibility visually reveals significant
146 differences between cell types by vascular site (**Fig 1D**). Analysis of RNA expression of
147 canonical genes to differentiate cell type shows strong correlation to overall gene
148 chromatin activity (e.g. *Myh11* — smooth muscle, **Fig 1E&F**). Integrated cell clusters
149 were then assigned to the major cell types of the vascular wall, vascular smooth muscle
150 cells (SMCs), fibroblasts, endothelial cells, and macrophages (**Fig 1G**) using known
151 lineage markers. To further focus on SMC and fibroblast cell populations, a subsetted
152 analysis of SMC and fibroblasts was performed with UMAP visualization of scRNAseq,
153 scATACseq, and integrated datasets, demonstrating clear separation of cells by original
154 vascular site, demonstrating a unique vascular site-specific chromatin and RNA profile
155 by cell type (**Fig 1H&I**).
156
157 ***Epigenomic patterns of vascular SMCs are cell type and vascular site specific***
158 UMAP clustering of SMCs from RNA, ATAC, and integrated datasets
159 demonstrate a pattern where SMCs from the ascending aorta, carotid artery, and
160 descending thoracic vascular sites are distinct from one another (**Fig 1H**). Chromatin
161 peak accessibility analysis between ascending and descending thoracic aorta SMCs
162 identifies 4,805 peaks which are differentially accessible (**Fig 2A**). Peak locations were
163 analyzed using Genomic Regions Enrichment of Annotations Tool (GREAT)[34]. GREAT
164 performs genomic region-gene associations by assigning a regulatory domain for each
165 gene, and then each genomic region is associated with all genes whose regulatory

166 domain it overlaps. Of these peaks, the majority (3,971/4,805; 83%) are associated with
167 2 genes within a region (**Fig 2B**, **Table S1**). A distribution of region-gene association
168 distances to TSS is observed where most peaks lie downstream of the TSS (**Fig 2C**).
169 Roughly 12% of region-gene associations are within 5kb of the TSS of a gene (**Fig 2C**)
170 and approximately 43% (4,496/8,789) of region-gene associations are within 50kb of a
171 TSS (**Fig 2C**).
172 When comparing peak accessibility between ascending and descending aorta,
173 specific chromatin regions are identified as having marked differential accessibility.
174 Among the top differentially accessible peaks in the ascending SMC population lie at
175 chr8-57320451-57321235 and chr14-63244897-63245811, 140bp and 83bp upstream
176 from the TSSs for *Hand2* and *Gata4* (**Fig 2D&E**). Coverage plots of chromatin
177 accessibility reveal *Hand2* regulatory regions to be open in ascending and carotid SMCs
178 while closed in descending SMCs (**Fig 2D**). This contrasts with regulatory regions of
179 *Gata4* that appear to be in an open state in the ascending SMC however in a largely
180 closed state in the carotid and descending SMCs (**Fig 2E**). Consistent with the role of
181 Hox genes during the development of somites, top peaks that have increased
182 accessibility in the descending aortic SMC include genomic regions that lie near the
183 *Hoxb* family of transcription factors (i.e. chr11-9686379-96287301 at *Hoxb7*, **Fig 2F**,
184 **Table S1**). Featureplots of peak accessibility for *Hand2* and *Hoxb7* peaks (**Fig 2G-I**)
185 highlight distinct differential accessibility dependent on SMC vascular site of origin.
186 Consistent with epigenetic marks, RNA expression analysis reveals *Hand2* expression
187 in the ascending and carotid SMC while absent expression in the descending SMC (**Fig**
188 **2J**). Top differential peak analysis identifies other cardiac and vascular development

189 genes that have higher chromatin accessibility within the ascending aorta include
190 *Tbx20*, *Tbx2*, *Gata4*, and *Wnt16*, while homeobox genes such as the *Hoxa/b/c* family of
191 genes, *Smad2*, and are identified as having higher chromatin accessibility within the
192 descending aorta (**Tables S2&S3**).

193 Evaluation of biological processes of differentially accessible chromatin regions
194 using GREAT identifies key development pathways that characterize the ascending
195 aorta SMC such as 'outflow tract morphogenesis', 'cardiac septum development', and
196 'embryonic heart tube development' as well as other pathways involving cellular
197 signaling such as 'transmembrane receptor protein signaling', 'regulation of Ras protein'
198 (**Fig S1A**). Biological processes that characterize the descending aorta SMC include
199 developmental programs such as 'anterior/posterior pattern specification', however
200 notable processes regulating cytoskeletal organization such as 'actin cytoskeleton
201 organization', 'actomyosin structure organization', and 'regulation of SMC
202 differentiation', as well as processes involved in the negative regulation of TGFβ
203 signaling such as 'negative regulation of TGFβ receptor signaling' (**Fig S1B**).

204 We then performed transcription factor motif accessibility analysis using
205 ChromVAR as previously described[35]. In comparing ascending versus descending aorta
206 SMCs, we identified that ascending SMCs have notable transcription factor motif
207 enrichment for AP1 factors (i.e. FOS:JUNB 'TGAGTCA', **Fig 2K**), neural crest and
208 secondary heart field transcription factors such as *HAND2*, *GATA4*, and *TCF21* (i.e.
209 *HAND2*, **Fig 2L**), as well as TFs with known roles in SMC differentiation such as
210 *TWIST1* and *TEAD* factors (**Table S4**). Top differentially accessible motifs in the
211 descending SMCs highlight GC rich KLF motifs (i.e. *KLF15*, **Fig 2M**), numerous AT rich

212 homeobox transcription factor motifs including HOX factors/Cdx1 (caudal type
213 homeobox 1)/Lhx1 (LIM homeobox 1), and MEF2 factors (i.e. *MEF2A*, **Fig 2N**, **Table**
214 **S5**). Motif enrichment analysis of the carotid SMCs suggest similarities to ascending
215 SMCs with notable enrichment for AP1 and *HAND2* motifs (**Table S6**), however we
216 identified additional motif enrichment that appeared to be largely distinct to the carotid
217 SMC including distal-less homeobox (DLX) motifs (*DLX5*, **Fig 2O**) as well as
218 neurodevelopmental E-box TFs such as *NEUROD1* and *NEUROG2* (*NEUROD1*, **Fig**
219 **2P**).
220 Gene expression analysis using FindMarker from scRNAseq data of SMCs
221 reveals 252 genes which have differential expression among vascular sites (147
222 ascending, 77 carotid, 28 descending) (**Table S7**) that largely match genes identified by
223 differential peak accessibility analysis (**Fig 2Q**). Top differentially expressed genes
224 within the ascending SMC population includes expected developmental genes such as
225 *Tbx20* and *Hand2* (**Fig 2Q**), secondary heart field marker *Tnnt2* (**Fig 2Q&R**), but also
226 numerous genes with previously demonstrated roles in atherosclerosis suggesting
227 vascular site-specific disease risk mechanisms (**Fig 2Q**), including *Ccn3* (cellular
228 communication network factor 3) which has previously reported vascular protective
229 effects by inhibiting neointimal formation and plaque development[36,37] and *Dcn* (decorin)
230 that has been shown to be protective in atherosclerosis[38]. Notably, we identify specific
231 vascular development and inflammation genes as having higher expression within
232 SMCs isolated from the carotid artery, such as *Klf4*, *Fosb*, *Jun*, and *Atf3* (**Fig 2Q&R**).
233 *Fosb* and *Jun* have specific roles in mediating cellular and arterial contractility[39], *Atf3* is
234 a CAD GWAS gene and has recently been identified to have vascular protective effect

235 in atherosclerosis[23], and *Klf4* has critical roles in mediating SMC phenotypic modulation
236 and promotes atherosclerosis[40]. Specific genes which have higher expression within the
237 descending thoracic SMCs include signal transduction genes such as *Rgs5* (Regulator
238 of G protein signaling 5) (**Fig 2Q**, **Table S7**), *Fn1* (fibronectin 1), and *Ccdc3* (coiled-coil
239 domain containing 3). *Rgs5* has been reported to be a specific marker of peripheral
240 arterial smooth muscle, is downregulated in atherosclerosis, and acts to inhibit SMC
241 proliferation and neointimal formation[41,42], *Fn1* is a putative CAD GWAS gene thought to
242 be protective in CAD and loss of function has been implicated in thoracic aortic
243 aneurysm[43,44], and *Ccdc3* has been found to inhibit TNFα mediated vascular
244 inflammation[45].
245
246 ***Fibroblast cell subset analysis reveals vascular site-specific gene programs and***
247 ***disease risk genes***
248 Evaluation of fibroblast subset population similarly reveals differences in
249 chromatin accessibility and gene expression across vascular sites (**Fig 1I**). Peak
250 accessibility analysis between fibroblasts from the ascending and descending aorta
251 reveals 7,008 peaks that are differentially accessible (**Fig 3A**, **Table S8**). Top peaks
252 that have higher accessibility in the ascending aorta include peaks located at chr9-
253 24773921-24774837 and chr14-63244897-63245811 that lie 95bp and 85bp upstream
254 from the TSSs of *Tbx20* and *Gata4* respectively, while peak chr15-57985530-57986444
255 is increased in both ascending and carotid and lies 568bp downstream from the TSS of
256 *Fam83a* (**Fig 3B-D**). Top peaks with higher accessibility in the descending aorta
257 fibroblast population includes peaks near Hox related family members (i.e. chr11-

258 96298662-96299576 at *Hoxb6*) (**Fig 3E**), however additional peaks include chr17-
259 35590469-35591345 in a gene desert 23,457bp downstream of noncoding RNA
260 2300002M23Rik, as well as chr8-114679333-114680184 that lies within an intron and
261 240,104bp downstream of the TSS of *Wwox* (**Fig 3F&G**). Featureplots of peak
262 accessibility to peaks that correspond to *Fam83a* and *Wwox* (chr15-57985530-
263 57986444 and chr8-114679333-114680184 respectively) highlight distinct vascular site-
264 specific chromatin accessibility (**Fig 3H&I**).
265 Peak to gene association analysis with GREAT reveals top genes with higher
266 peak accessibility in the ascending aorta to include expected key developmental genes
267 such as *Tbx20*, *Gata4*, *Tcf21*, and *Hand2*, as well as signaling genes such as *Fam83a*,
268 *Cul4b*, and *Cdkn2b* (**Table S9**). Peaks with higher accessibility within the descending
269 aorta include peaks that lie near the *Hoxa/b/c* family of transcription factors as well as
270 other developmental transcription factors such as *Pax1* and *Foxd1* (**Table S10**). Gene
271 ontology pathway analysis using GREAT identifies top pathways to be enriched in the
272 ascending aorta to include developmental pathways such as 'cardiac septum
273 morphogenesis' and 'embryonic heart tube development', but also pathways that
274 suggest a distinct response to TGFβ such as 'regulation of TGFβ receptor signaling'
275 and 'regulation of cellular response to TGFβ stimulus' (**Fig S2A**). Pathways enriched
276 within the descending aorta fibroblast include an enrichment of pathways involved in
277 extracellular structure organization such as 'extracellular matrix organization', 'collagen
278 fibril organization', and 'negative regulation of cell-cell adhesion' (**Fig S2B**).
279 Motif accessibility analysis using ChromVar within fibroblast populations reveals
280 ascending fibroblasts to have a marked increase in accessibility of *TCF21* and other

281 bHLH family of transcription factors, similar to what was observed in the SMC
282 ascending population (**Fig 3J&K**, **Table S11**). However, motif enrichment appears to
283 further identify regulators of TGFβ signaling including the SMAD2:3:4 and TGIF1 motifs
284 (**Fig 3L**). *SMAD3* is a member of the TGFβ superfamily and has causal roles in
285 aneurysm[46] and coronary artery disease[47]. Like that observed in the SMC, descending
286 aortic fibroblast appear to have increased accessibility of motifs that relate to homeobox
287 transcription factors such as HOX family of TFs (i.e. *HOXA13*, **Fig 3M**), *MEIS1/2*, GC
288 rich KLF family members, as well as *SOX9* and other SOX TFs further appear enriched
289 in the descending fibroblasts (**Fig 3N**, **Table S12**). Motif enrichment for carotid fibroblast
290 appear to show a distinct increase in accessibility to developmental TF *NKX6-1* (**Fig**
291 **3O**) as well as related TFs with similar sequence (i.e. *MEOX1/2*)(**Table S13**).
292 RNA expression analysis between vascular sites demonstrates significant
293 concordance with peak accessibility analysis. Fibroblast specific gene expression
294 analysis reveals 597 genes which have differential expression between vascular sites
295 (314 ascending, 149 carotid, 134 descending)(**Fig 3P**, **Table S14**). The top 10 genes
296 which differentiate vascular sites include expected development genes such as *Tbx20*,
297 *Tcf21* (ascending), *Igfbp4*, *Sod3* (carotid), and *Hox*a7, *Col1a2* (descending)(**Fig 3Q**). A
298 notable observation is that descending fibroblasts appear to be enriched for
299 extracellular structure organization pathways by scATACseq (**Fig S2B**) and by RNA we
300 observe a pattern of increased expression of collagen extracellular matrix genes (**Fig**
301 **3Q&R**). These genes overlap with known causal genes for hereditary thoracic
302 aortopathy (HTAD) and loci associated with aortic dimension and aortic dissection
303 risk[48,49]. Evaluation of these genes reveal a pattern where TGFβ related HTAD genes in

304 which gain of function leads to disease (i.e. *TGFBR1/2*, *TGFB2*, *SMAD3*) show
305 increased expression in the ascending fibroblasts, while collagen and matrix related
306 HTAD and other collagen genes where loss of function leads to disease (i.e. *FBN1*,
307 *COL3A1*, *LOX*) there is decreased expression (**Fig 3R**). This suggests distinct
308 regulation of extracellular matrix and TGFβ signaling genes in fibroblasts in a vascular
309 site-specific manner that may suggest a relationship to risk of thoracic aortic disease.
310

311 ***Endothelial cell subset analysis shows distinct vascular site-specific chromatin***
312 ***accessibility***

313 Single cell analysis of endothelial cell subset population reveals vascular site-
314 specific chromatin accessibility and gene expression programs. Visualization with
315 UMAP demonstrates separation of endothelial cells from the ascending aorta with
316 somewhat less pronounced differences between endothelial cells from the carotid artery
317 and descending aorta based on RNA, ATAC, and integrated datasets (**Fig 4A-C**). Peak
318 accessibility analysis between endothelial cells from the ascending and descending
319 aorta identifies 935 peaks with differential accessibility meeting significance using an
320 adjusted P value of 0.05 (**Fig 4D**) with 14,388 peaks meeting an unadjusted P value of
321 0.05 (**Table S15**). Top peaks that have increased accessibility in the ascending aorta
322 includes peak chr6-134981212-134982145 which lies 39bp upstream of the TSS of
323 *Apold1* (**Fig 4E&F**). *Apold1* (apolipoprotein L domain containing 1, aka VERGE) has
324 been previously reported as an endothelial cell specific stress response gene and
325 protects against vascular thrombosis[50,51]. Peak analysis further highlights peaks related
326 to Wnt signaling including peak chr6-18031351-18032250, which lies 1216bp upstream

327 of the TSS for *Wnt2* (**Fig 4G**). Coverage plot of this genomic region demonstrates that
328 chromatin accessibility is nearly entirely closed in the descending aorta with only minor
329 accessibility in the carotid (**Fig 4G**). Notably, the descending aorta endothelial cells
330 have increased accessibility of Hox related genes (i.e. peak chr6-52225707-52226553,
331 *Hoxa9*)(**Fig 4H&I**), as well as peaks related to genes involved in Notch signaling such
332 as chr2-137109516-137110365 which lies 6707bp downstream of the TSS for *Jag1* (**Fig**
333 **4J**) where coverage plot of this genomic region reveals differential peak accessibility
334 with carotid and descending endothelial cells having similar accessibility (**Fig 4J**). *Jag1*
335 (jagged 1) and associated Notch pathway signaling has important roles in suppressing
336 vascular smooth muscle chondrogenic fate and in the formation of the atherosclerotic
337 fibrous cap[52,53].

338 Motif accessibility analysis was performed comparing ascending and descending
339 aortic endothelial cell populations. Top differentially accessible motifs in the ascending
340 endothelial cells highlight *LEF1* (**Fig 4K**, **Table S16**). *LEF1* plays a critical role in Wnt β-
341 catenin signaling and regulates endothelial cell fate specification[54]. Other motifs
342 enriched in the ascending population including *Hand2* as well as multiple ETS factors
343 (**Table S16**). ETS factors play important roles in cellular growth and differentiation and
344 regulate vascular inflammation and remodeling where inhibition of ETS transcription
345 factors promotes vessel regression[55,56]. Top motifs enriched in the descending aortic
346 endothelial cells highlights *NFIC* (**Fig 4L**, **Table S17**) where motif accessibility appears
347 to be enriched in both the carotid and descending endothelial cells. Other motifs include
348 multiple Hox family members, TEAD family members, and other nuclear factors such as

349 *NFIX* (**Table S17**). Motif enrichment in carotid endothelial cells highlights nuclear factors
350 such as *NFIA/C/X* as well as AP1 factors (**Table S18**).
351 Differential gene expression analysis reveals specific patterns differentiating
352 endothelial cell programs by vascular site (**Fig 4M**) with FindMarker analysis identifying
353 397 differentially expressed genes between vascular sites (174 ascending, 127 carotid,
354 96 descending) (**Table S19**), where heatmap analysis suggests greater similarity
355 between carotid and descending endothelial cells compared to ascending (**Fig 4M**).
356 Ascending aortic endothelial cells have increased expression of VEGF receptors *Kdr*
357 (kinase insert domain receptor, aka VEGFR), *Flt1* (fms related receptor tyrosine kinase
358 1, aka VEGFR1), and *Flt4* (fms related receptor tyrosine kinase 4, aka VEGFR3)
359 (Figure 4N&O). Descending aortic endothelial cells have notable increase in expression
360 of *Edn1* as well as other BMP factors (i.e. *Bmp4*) as well as interestingly xenobiotic
361 transformation gene *Cyp1b1* (cytochrome p450, 1b1) (**Fig 4P&Q**). Vascular site-specific
362 expression of *Cyp1b1* is particularly notable as it contributes to abdominal aortic
363 aneurysm and suggests a vascular site-specific mechanism of aneurysm[57,58]. Carotid
364 endothelial cells have higher expression of specific genes that appear to play unique
365 roles within the cerebral vasculature such as *Efemp1* (EGF containing fibulin
366 extracellular matrix protein 1) (**Fig 4R**) an extracellular matrix glycoprotein which
367 regulates vessel development and has been associated with intracranial vascular
368 disease and white matter density through large genome wide association studies[59].
369
370 ***Macrophage cells have minimal epigenomic and transcriptional variation across***
371 ***vascular sites***

372 Given the significant vascular site-specific epigenomic and RNA transcriptional
373 profiles observed within vascular SMCs, fibroblasts, and endothelial cells, we next
374 evaluated if resident macrophages within healthy vascular tissues harbor specific
375 epigenomic and transcriptional profiles. Macrophage cells from integrated
376 scATACseq/scRNAseq data were subsetted and subsequently analyzed. Importantly,
377 UMAP visualization of macrophage cells with RNA, ATAC, and integrated datasets
378 reveals no significant differences in macrophage cells across vascular sites (**Fig S3A-**
379 **C**). Differential peak accessibility analysis between ascending and descending aorta
380 macrophages do not reveal any peaks which meet statistical significance as
381 differentially accessible (**Fig S3D**). Differential gene expression analysis with scRNAseq
382 data reveal very minimal differences in gene expression (**Fig S3E**). This lack of vascular
383 site-specific macrophage diversity across the aorta is notable given the contrasting
384 finding within SMCs, fibroblasts, and endothelial cells, and that significant leukocyte
385 diversity develops within the aorta during atherosclerosis[60].
386
387 ***Cell type and vascular site-specific gene regulatory networks highlight distinct***
388 ***ascending fibroblast regulatory networks***
389 These data indicate that epigenomic landscape is not only cell type but vascular
390 site-specific with key differences in transcription factor motif accessibility. To further
391 understand how TF regulatory elements may further control gene expression on a cell
392 type and vascular site-specific basis, we utilized this multi-modal single-cell data to infer
393 gene regulatory networks (GRNs) with Pando[61]. By integrating scRNA and scATAC
394 datasets and subsetting across vascular cell type and vascular site of origin, we utilized

395 Pando to infer GRNs through modeling gene expression with understanding the
396 interaction of TF expression with TF binding sites and gene targets (**Fig 5A**). With
397 Pando, we initiated GRN analysis by scanning candidate genomic regions and identified
398 TF binding motifs to then infer GRN modules. To understand how regulatory networks
399 may differ within cell type based on vascular site, we identified TF modules for aortic
400 SMCs and Fibroblasts in both ascending and descending aortic sites. In these modules,
401 we identified GRN TF and TF gene targets. In the SMC population, we identified 37 and
402 38 TF modules in the ascending and descending cells, respectively. In the fibroblast
403 population, we identified 56 and 40 TF modules in the ascending and descending cells,
404 respectively (**Fig 5B&C**). In both SMC and fibroblast cell populations, the majority of TF
405 modules appear to be shared between ascending and descending cells (**Fig 5B&C**),
406 with key TFs including *Atf3*, *Creb5*, *Fosb*, *Klf2/4/6*. However, although SMC TF modules
407 show relatively equal proportion of TF modules that are distinct to ascending and
408 descending, ascending fibroblasts appear to have a notable increase in distinct TF
409 modules (20 vs 4) (**Fig 5C**). Distinct ascending fibroblast GRN TF modules include
410 *Meox1*, which has recently been described as a master regulator of fibroblast activation
411 in cardiac fibroblasts through epigenetic mechanisms[20]. GRN TF gene targets appear to
412 have less overlap between ascending and descending cell populations in both SMCs
413 and fibroblasts (**Fig 5D&E**), however consistent with GRN TF modules, there is a
414 greater proportion of ascending fibroblast GRN gene targets compared to descending
415 (108 vs 43) (**Fig 5D&E**). Visualization of ascending fibroblast GRN highlights the
416 proximity of *Meox1* to other developmental TFs *Tbx20* and *Gata4* (**Fig 5F**). Other

417 distinct fibroblast ascending GRN TF modules include *Tcf21*, *Irf7/8*, *Sox4/7/17*, and
418 *E2f8*.
419
420 ***Vascular site-specific Meox1 activation implicates epigenetic 'priming' for***
421 ***fibroblast activation in ascending aortic fibroblasts***
422 Our findings implicate a cell type and vascular site-specific 'epigenetic memory'
423 of important regulatory enhancer elements with functional effect on disease relevant
424 pathways. A notable observation from evaluation of GRNs is that ascending fibroblasts
425 have increased proportion of distinct regulatory networks from descending fibroblasts
426 highlighting the TF *Meox1*. We interrogated our scRNAseq and scATACseq fibroblast
427 integrated dataset where we see that *Meox1* has increased RNA expression in
428 ascending fibroblasts, but this expression is largely limited to a specific cell population
429 that represents valvular fibroblasts (**Fig 5G&H**). Importantly, we see that *Meox1*
430 chromatin accessibility is much more expansive and extends throughout all ascending
431 and includes carotid fibroblasts, with increased total chromatin accessibility in the
432 ascending/carotid fibroblast populations (**Fig 5I**). This discrepancy of chromatin
433 accessibility and RNA expression for non-valvular ascending fibroblasts may suggest
434 evidence to support an epigenetic 'priming'.
435
436 ***Primary adventitial fibroblast response to TGFβ is dependent on vascular site and***
437 ***implicates functional developmental epigenomic memory***
438 We have shown that vascular SMCs, fibroblasts, and endothelial cells have
439 transcriptional and epigenomic features that are distinct to vascular site. Further, TF

440 motif accessibility analysis in fibroblasts reveals an increased accessibility of *AP1*, and
441 *SMAD2:3:4*, and *TCF21* motifs in the ascending fibroblast population compared to
442 carotid and descending fibroblasts (**Fig 3**), with further gene regulatory network analysis
443 suggesting distinct regulatory TF module activity in ascending fibroblasts highlighting
444 master regulator of fibroblast activation *Meox1* (**Fig 5**). This differential chromatin
445 accessibility would suggest the potential for heightened biological response to TGFβ in
446 ascending fibroblasts. To evaluate the functional effect of this differential chromatin
447 accessibility and to identify if differential gene expression is retained following removal
448 from vascular site flow conditions, we isolated and cultured primary adventitial
449 fibroblasts from healthy 14 week old C57BL/6 mice from the ascending and descending
450 aorta, passaged cells 3X allowing for separation from hemodynamic effects, and
451 stimulated them with control or TGFβ (10ng/mL, 48hrs) and performed bulk RNA
452 sequencing (n = 3 per condition) (**Fig 6A**).
453 Principal component analysis (PCA) of RNAseq data reveals distinct separation
454 of samples based on origin of vascular site and stimulation with TGFβ (**Fig 6B**). Upon
455 evaluation of differential gene expression by vascular site, we observe 1342
456 differentially expressed genes between ascending and descending fibroblasts (**Fig 6C**,
457 **Table S20**). Ascending fibroblasts have increased expression of genes including
458 *Hand2*, *Tbx20*, *Pcolce2*, *Tcf21*, and *Gata4* (**Fig 6C**, **Fig S4A**), while descending
459 fibroblasts have increased expression of *Hox* family of genes (i.e. *Hoxb9*, *Hoxa7*,
460 *Hoxc8*), *Col6a3*, and *Pax1* (**Fig 6C**, **Fig S4B**). When evaluating response to TGFβ
461 stimulation, comparing all samples by TGFβ treatment, we identify 4,234 DE genes,
462 with top upregulated genes including *Ada*, *Snx30*, *Wisp1*, *Cthrc1*, *Loxl2*, and *Akap5*,

463 while top downregulated genes include *Adm*, *Gstm1*, *Mcc*, *Rras2*, *Il6ra*, and *Vegfd* (**Fig**
464 **6D, Table S21**). To evaluate the effect of TGFβ by vascular site, we compared the
465 transcriptomic effect of TGFβ stimulation within ascending and descending fibroblast
466 samples. We identify TGFβ stimulation to induce a markedly higher transcriptional effect
467 in ascending fibroblasts, with 6,733 DE genes (**Fig 6E**, **Table S22**) while only 2,250 DE
468 genes within descending fibroblasts (**Fig 6F**, **Table S23**).
469 By performing an interaction analysis, we reveal key genes with differential
470 response to TGFβ by vascular site. In this analysis, 422 genes meet FDR cutoff for
471 interaction significance (**Fig S5**, **Table S24**). When plotting the log2FC_interaction
472 (log2FC > 0 represents greater effect TGFβ in ascending; log2FC < 0 represents
473 greater effect TGFβ in descending), we identify that matrix gene *Eln* is the top
474 interacting gene that has much lower expression in descending fibroblasts but is rapidly
475 upregulated in response to TGFβ (**Fig S5A&B**). Here, we identify that *Meox1* has a
476 marked interaction in response to TGFβ with greater effect in ascending fibroblasts,
477 where although low expression of *Meox1* is present in ascending fibroblasts, *Meox1*
478 expression significantly increases with TGFβ treatment, an effect not seen in
479 descending fibroblasts (**Fig S5C**). This relationship also includes other TGFβ response
480 genes such as *Gdf6* that are more highly induced in ascending fibroblasts, while *Tgfb1*
481 and *Tgfb3* are more induced in descending fibroblasts (**Fig S5C**, **Table S24**). Numerous
482 collagen genes have differential response to TGFβ by vascular site, where *Col8a1* and
483 *Col5a2* are upregulated by TGFβ to a greater extent in descending fibroblasts (**Fig**
484 **S5D**). Alternatively, *Col28a1* and *Col6a1* are downregulated by TGFβ to a greater
485 extent in descending fibroblasts (**Fig S5D**). TFs such as *Klf4* and *Ptx3* are more highly

486 expressed in ascending fibroblasts and then downregulated by TGFβ to a greater extent
487 than descending fibroblasts (**Fig S5E**). However, *Ahr* is downregulated by TGFβ in
488 descending fibroblasts only while *Hoxb5* shows differing effects by vascular site, where
489 it is modestly upregulated in ascending while downregulated in descending fibroblasts
490 (**Fig S5E**).

491 By evaluating the 200bp DNA sequence upstream of the TSS of differentially
492 expressed RNA transcripts in ascending versus descending fibroblast comparison, we
493 evaluated TF motif enrichment using HOMER[62]. In control samples, DE genes
494 upregulated in ascending vs descending fibroblasts reveal enrichment of key TFs
495 including SMAD3 (TWGTCTGV), KLFs including KLF4 (GCCACACCCA), FOS
496 (NDATGASTCAYN), and HIF1α (TACGTGCV)(p-values 1.0E-10, 1.0E-13, 1.0E-07, and
497 1.0E-05, respectively). DE genes upregulated in descending fibroblasts reveal
498 enrichment of TFs including HOXA11 (TTTTATGGCM), HOXA9 (RGCAATNAAA),
499 HOXC6 (GGCCATAAATCA), (p-values 1.0E-07, 1.0E-06, 1.0E-03, respectively) (**Fig**
500 **6G**). We then similarly evaluated the motif enrichment of the 200bp sequence upstream
501 of the TSS of upregulated genes in ascending fibroblasts in response to TGFβ and then
502 for descending fibroblasts in response to TGFβ (**Fig 6H&I**). In this comparison, although
503 motif enrichment to TGFβ has similarities between ascending and descending
504 fibroblasts with GC rich motifs such as SP2/5 and KLF factors similarly enriched (**Fig**
505 **6H&I**), distinct differences emerge. Ascending fibroblast response to TGFβ motif
506 enrichment highlights AP1 factors, SMAD3, as well as MEF2 factors (**Fig 6H**). In the
507 descending fibroblast response to TGFβ highlights ETS factors and other NRF factors
508 and to a lesser extent AP1 factors (**Fig 6I**). However SMAD3 and MEF2 factors are not

509 identified as being enriched. The differential enrichment of these TFs in differentially
510 expressed genes between vascular site and in response to TGFβ suggests this
511 differential chromatin accessibility to have functional effect on global transcriptome.
512

513 ***Aortic dimension GWAS identifies genes with vascular site-specific expression***

514 Our data indicates that epigenomic landscape are not only cell type, but vascular
515 site-specific. However, it is unclear if these vascular site-specific enhancers and gene
516 programs relate to human genetic evidence of disease. To evaluate this question, we
517 leveraged the data from a recently performed GWAS to understand the genetic
518 determinants of ascending versus descending aortic dimension[17]. Through an algorithm
519 based method to evaluate cardiac MRI imaging of UK Biobank participants, Pirrucello et
520 al. (2022)[17] identified 82 and 47 genomic loci which met genome wide significance for
521 ascending and descending aortic dimensions, respectively. We hypothesized that if
522 vascular site-specific regulatory enhancers influence genetic disease risk, that we would
523 observe aortic dimension GWAS genes to be differentially expressed in a vascular site-
524 specific manner. By taking the nearest gene for each locus, we evaluated if these
525 GWAS genes are enriched in the ascending versus descending differentially expressed
526 RNA gene lists for each cell type (SMC, Fibro, Endo). Following performing a differential
527 gene expression analysis between ascending and descending aortic SMC, Fibro, and
528 Endo, cell types, we evaluated the proportion of GWAS aortic dimension genes to be
529 differentially expressed. We observed that these GWAS genes are enriched in the
530 differential gene analysis within SMC, Fibroblasts, and Endothelial cells. In SMCs, 25%
531 (21/82) and 21% (10/47) of ascending and descending aortic dimension GWAS genes

532 are differentially expressed (*p=5.4E-6* and *p=2.5E-4*, compared to random gene
533 set)(**Fig 7A-C**). In Fibroblasts, 32% (26/82) and 34% (16/47) of ascending and
534 descending aortic dimension GWAS genes are differentially expressed (*p=9.9E-5* and
535 *p=1.8E-4*, compared to random gene set)(**Fig 7D-F**). Whereas, in endothelial cells, 15%
536 (12/82) and 17% (8/47) of ascending and descending aortic dimension GWAS genes
537 are differentially expressed (*p=0.024* and *p=0.019*, compared to random gene set)(**Fig**
538 **7G-I**). These data highlight that a large proportion of genes that regulate aortic
539 dimension are differentially expressed across vascular sites within a cell type and
540 possibly suggests fibroblasts to be a primary cell type.
541
542 ***ChromBPnet predicts human genotype effect of chromatin accessibility in a cell***
543 ***type and vascular site-specific manner***
544 These data indicate that genes for which variants regulate aortic dimension have
545 not only cell type but vascular site-specific expression and epigenomic patterns. This
546 may suggest that a gene variant can have a differing effect on TF motif binding,
547 chromatin accessibility, and gene regulation in not only a cell type but a vascular site-
548 specific context. To better understand this vascular site-specific epigenomic regulation,
549 we aimed to predict how a gene variant that influences aortic dimension (Pirruccello et
550 al., 2022)[17] may affect chromatin accessibility in a cell type and vascular site specific
551 manner using ChromBPNet[63]. ChromBPNet is a novel, bias factorized, base-resolution
552 deep learning model of chromatin accessibility[63]. Prior training of the ChromBPNet
553 model has been predicated on the concept that gene variants affect TF binding of cis-
554 regulatory elements (cREs) in a cell context-specific manner[63]. Training of a

555 convolutional neural network (CNN) for ChromBPNet has utilized chromatin accessibility
556 data across 5 ENCODE Tier 1 cell lines[63], however, although this takes into account
557 how a variant may affect TF binding and chromatin accessibility within cell type, it does
558 not allow for the investigation of a variant effect within cell type but across vascular
559 sites. To overcome this barrier, we utilized our multiomic single cell RNA and ATAC
560 sequencing data and trained the ChromBPNet model in 9 different groups (Ascending
561 aorta, Carotid, and Descending aorta, within SMC, Fibroblasts, and Endothelial cells) in
562 our mouse dataset. Given this 'genome-agnostic' approach, this model can predict the
563 fundamental effect of base pair change on chromatin accessibility. These individual cell
564 type and vascular site-specific models can then be applied to the human genome. We
565 leveraged the variants identified from the prior GWAS on aortic dimension[17], performed
566 linkage disequilibrium (LD) expansion to identify SNPs in LD with lead SNPs, and used
567 each of the 9 models to score variant effect for 27,556 variants based on cell type and
568 vascular site. We identified 469 high scoring aorta diameter LD-expanded GWAS
569 variants across all of the vascular site datasets (example, rs2959350, in LD with lead
570 SNP rs55736442 at *ANGPT1* locus, chr8:107367260:G:A, Ascending Endothelial cells,
571 **Fig 8A**). In this model, the variant allele has a pronounced activating effect on
572 chromatin accessibility across a ~300bp region.
573 For each variant, we scored the absolute log fold change (abs_logFC) from
574 variant effect as well as the p-value of the abs_logFC (abs_logFC.pval). To understand
575 how predicted variant effect may vary within cell type across vascular site, we first
576 evaluated the abs_logFC.pval and compared between ascending and descending SMC
577 models (**Fig 8B**). This reveals significant variation in p-value of logFC for a given SNP

578 between vascular sites (**Fig 8B**). However, upon evaluation of the variation of
579 abs_logFC for each SNP within SMC across vascular site, variation is significantly
580 reduced (**Fig 8C**). A similar level of variation of variant effect is seen when comparing
581 ascending and descending fibroblast and endothelial cell models (**Fig 8D&E**). To
582 understand the predicted variant effect between cell types, we then compared the
583 predicted abs_logFC in ascending SMC vs Fibro, SMC vs Endo, and Fibro vs Endo (**Fig**
584 **8F-H**). We observe a consistent pattern of a greater degree of variation in comparing
585 between cell types as opposed to within cell type across vascular site, consistent with
586 an overall understanding that variant effect is primarily influenced by cell type, however
587 within cell type, vascular site continues to have significant variant effect.
588 Following linear regression analysis of the abs_logFC within cell type between
589 ascending and descending models (i.e. Asc SMC vs Desc SMC), we identified the top
590 1% of deviant SNPs (furthest away from linear regression line). These top 1% deviant
591 SNPs highlight specific variants that appear to have vascular site-specific effect. For
592 example, rs11677932 is the lead SNP (chr2:237315312:G:A) at the *COL6A3* locus, a
593 gene we have previously highlighted as having differential expression within cell type
594 across vascular site. The variant effect is predicted to lead to epigenetic silencing;
595 however, this effect is greatest in SMC, compared to fibroblast and endothelial cells,
596 and within SMCs, this effect is greatest in descending SMC compared to ascending
597 SMC (**Fig 8I**).
598 The identification of variants that have vascular site-specific effects on chromatin
599 accessibility may suggest that variants can change pioneer TF binding to motifs that
600 influence vascular site-specific epigenetic patterns. To better understand these variants

601 and the potential TF motifs that they regulate, we took the top 1% of deviant SNPs away
602 from the linear regression, and from these SNPs, we selected a 200bp genomic window
603 (+/- 100bp around each SNP) and performed unbiased Motif Discovery function with
604 MEME Suite[64]. Known motif analysis of top discovered motifs was then performed using
605 TOMTOM (HOCOMOCOv11)[65]. This analysis was performed for top deviant SNPs in
606 SMC, fibroblast, and endothelial cell populations, and here, we identified novel motifs
607 enriched in the genomic regions of these SNPs with differential effect on vascular site.
608 TOMTOM analysis of discovered motifs revealed numerous TF motifs that we have
609 similarly identified as having differential motif accessibility between vascular sites. For
610 example, analysis of top discovered motif from SMC data reveals motif enrichment for
611 *MEF2A/C*, consistent with our prior finding of enriched *MEF2A/C* motif in descending
612 SMC (**Fig 8J**). Similarly, in analysis of the top discovered motif from fibroblast data, we
613 observe an enrichment for multiple zinc finger motifs including *IKZF1* and *ZN250*,
614 however we also see an enrichment for *TEAD4* (**Fig 8K**), a motif we have previously
615 observed to have differential accessibility. Further, in the second top motif in this
616 fibroblast data, we observe an enrichment for a *SMAD3* motif (**Fig 8L**), consistent with
617 our previously observed increased in *SMAD3* motif accessibility in ascending aortic
618 fibroblasts. Finally, evaluation of these SNPs from endothelial data further reveals a
619 discovered motif that is notably enriched for a *HAND2* motif (**Fig 8M**), a motif we had
620 similarly seen enriched in ascending aortic cell types. These data suggest that variants
621 that have differential effect on chromatin accessibility between vascular sites lie in
622 genomic regions enriched for motifs that have differential accessibility between vascular

623 sites. These data further support our hypothesis that vascular site-specific epigenomic
624 patterns influence human genetic determinants of vascular disease risk.
625
626 **Discussion**
627 Chromatin architecture and cis-regulatory elements such as enhancers and
628 promoters are critical in mediating cellular gene programs in a cell type specific
629 manner[19]. Disease associated gene variants identified through GWAS are now
630 increasingly being recognized to influence disease risk through modification of these
631 regulatory regions of the genome[66]. Additionally, there is now growing experimental
632 evidence that vascular disease associated gene loci influence disease risk in cell type
633 specific mechanisms, where common human genetic variation can modify the function
634 of cell type specific enhancers[22,23]. Risk of vascular diseases, such as atherosclerosis,
635 aneurysm, or autoinflammatory vasculitides, are vascular site-specific, with disease
636 associated genetic loci suggesting differing genetic mechanisms of disease. These
637 observations raise the question as to what extent do cell type specific enhancers and
638 gene programs vary by vascular site, and do these variations contribute to disease risk?
639 Here, we evaluated cell type and vascular site-specific enhancer and gene
640 expression profiles of healthy vascular tissue in adult mice from three disease relevant
641 vascular sites, 1) ascending aorta and aortic root, 2) brachiocephalic and right common
642 carotid arteries, and 3) descending thoracic aorta (**Fig 1A**). These vascular sites
643 represent the developmental diversity that makes up the aorta, with these regions
644 arising from the secondary heart field and neural crest, neural crest, and somitic
645 mesoderm, respectively. This work has revealed thousands of differentially accessible

646 enhancers within vascular smooth muscle, fibroblasts, and endothelial cells. Through
647 use of this single cell epigenomic and transcriptomic multi-omic data, computational
648 analysis of gene regulatory networks, *in vitro* culture of primary aortic fibroblast cells,
649 and by using a novel machine learning approach to train and predict gene variant effect
650 on chromatin accessibility across vascular sites in the human genome (ChromBPNet),
651 we have defined an important observation — that epigenomic patterns are not only cell
652 type but vascular site specific. This data supports our understanding that gene variants
653 appear to regulate chromatin accessibility through influencing pioneer TF motif binding
654 of key TF (i.e. *SMAD3*, *MEF2A/C*, *HAND2*, *TEAD4*) in a vascular site-specific
655 mechanism. These data have important implications for our understanding of vascular
656 site-specific disease risk and may give insight into novel mechanisms of disease.
657 The activation of key developmental transcription factors is crucial in the
658 coordinated cellular development of the fetal and adult vasculature. Although
659 expression of genes such as *Hand2*, *Tbx20*, *Gata4*, *Wnt* and those encoding related
660 WNT signaling molecules, and *Hoxa/b/c* family of transcription factors have previously
661 been known to mediate vascular development[5,8,25-28], the residual chromatin
662 accessibility and gene expression of these developmental transcription factors in the
663 adult vasculature has been less well characterized. A notable observation of our study
664 is that key regulatory enhancers of development genes *Tbx20*, *Hand2*, and *Gata4* have
665 increased chromatin accessibility in the ascending aorta and carotid artery in
666 comparison to the descending aorta in smooth muscle and fibroblasts (**Figs 2&3**).
667 Whereas *Hoxb* and *Hoxa/Hoxc* family of transcription factors have increased chromatin
668 accessibility in the descending aorta (**Figs 2&3**). Although it is possible that

669 hemodynamic factors may be contributing to these epigenetic differences across
670 vascular sites, our data from culturing primary adventitial fibroblasts *in vitro* suggests
671 that these transcriptomic patterns are retained even when culturing in a dish and across
672 3 passages (**Fig 6**). These findings suggest that these vascular cells retain an
673 epigenetic 'memory' of their developmental program, suggesting these cells are poised
674 to turn on these gene programs.

675 This finding further raises the question as to the role of these development genes
676 in mediating vascular disease risk in adulthood. Although genetic variation in *TBX20*
677 has been associated with a spectrum of congenital cardiac lesions relating to cardiac
678 and vascular development[67], there have been increasing observations that genetic loci
679 near *TBX20* meet genome wide significance for disease in adulthood including coronary
680 artery disease[68], myocardial infarction[69], blood pressure[70], and aortic dimension and
681 distensibility[17,71]. Similarly, variants near *GATA4* and members of the *HOXB* family of
682 transcription factors such as *HOXB7* have been associated with hypertension[72,73], while
683 *HAND2* variants are associated with aortic dimension and atrial fibrillation[17,74]. The
684 vascular site and cell type-specific chromatin accessibility observed in our study of
685 these developmental transcription factors may suggest their ongoing role in mediating
686 vascular disease in adulthood in a vascular site-specific mechanism. This hypothesis of
687 developmental TFs involved in vascular disease pathogenesis has been similarly
688 supported by work from our lab on developmental TFs *TCF21* and *ZEB2*[22,32]. These
689 TFs — which have important roles in vascular development, regulating cell state
690 transitions and endothelial to mesenchymal transition[75,76] — have been identified
691 through GWAS as having additional roles in the development of CAD[12,77]. SMC specific

692 deletion of *Tcf21* and *Zeb2* in the mouse revealed a significant effect on transcriptional
693 regulation, epigenetic landscape, and plaque characteristic, further defining their roles
694 as causal CAD genes[22,32].
695 TF motif accessibility analysis identified an important observation that
696 *SMAD2:SMAD3* motif is enriched in ascending aortic fibroblasts, highlighting a potential
697 vascular site-specific response to TGFβ signaling. It was first identified nearly 30 years
698 ago in chick embryos that vascular SMCs derived from the neural crest have enhanced
699 response to TGFβ signaling compared to ectoderm derived SMCs[78,79]. More recently,
700 transcriptomic differences across vascular sites and organ specific fibroblast
701 transcriptomic identity has been reported[30,80]. However, epigenomic landscape and
702 differential motif accessibility across vascular sites has not been reported. By isolating
703 and culturing primary adventitial fibroblasts from ascending and descending aorta, *in*
704 *vitro* experiments with TGFβ stimulation with bulk RNA sequencing confirmed that
705 differential gene expression by vascular site is retained following isolation and *in vitro*
706 culture and revealed ascending fibroblasts to have a markedly greater response to
707 TGFβ than descending fibroblasts (**Fig 6**), and motif accessibility analysis of
708 differentially expressed genes further suggests distinct response to AP1 factors such as
709 JUN, SMAD2/3, and MEF2 factors (**Fig 6H**). These are two important observations that
710 reveals 1) DE genes by vascular site in fibroblasts are independent of differential
711 laminar and turbulent flow and 2) implicates differential chromatin accessibility and
712 relevant TF motif accessibility to have causal biological and disease relevant function.
713 Evaluation of GRNs on a cell type and vascular site-specific basis highlights the
714 ascending aortic fibroblasts to have a notable activation of *Meox1* as a key GRN TF

715 (**Fig 5**). *MEOX1* is a master regulator of fibroblast activation *Meox1*[20] and we further
716 identified an epigenetic 'priming' of key disease relevant genes. Primary fibroblast
717 culture shows similar baseline RNA expression of *Meox1* between vascular sites, but
718 *Meox1* is upregulated to a much greater extent in ascending fibroblasts in response to
719 TGFβ (**Fig S5C**), consistent with epigenetic priming and activation of key vascular site-
720 specific GRN.

721 Prior work has discovered that genomic variants identified through GWAS have
722 cell type specific effects, however, understanding if gene variants may have not only a
723 cell type but vascular site-specific effect is challenging to determine. Our data here
724 highlights that many of the GWAS genes identified from a recent aortic dimension
725 GWAS[17] are differentially expressed when comparing ascending versus descending
726 aortic SMC, fibroblasts, and endothelial cells, with a notable enrichment of these genes
727 in the fibroblast DE gene analysis (**Fig 7**). However, to understand how these variants
728 may regulate chromatin accessibility on a base pair resolution, we applied a unique
729 model, where by training a ChromBPNet model in each cell type and vascular site, we
730 employed 9 distinct models to predict variant effect of aortic dimension on a cell type
731 and vascular site-specific context. This work revealed that although cell type remains
732 the primary influence on chromatin accessibility, vascular site is an important influence.
733 Our work further highlights that variants that appear to modify effect based on vascular
734 site are enriched for genomic positions that have key TF motifs, suggesting that these
735 variants may modify the binding of TFs such as *SMAD3*, *MEF2A* and others and
736 regulate disease risk in a vascular site-specific mechanism (**Fig 8**).
737

738 **Limitations**

739 In this study, our aim was to evaluate single cell enhancer and transcriptional
740 profiles across vascular sites in healthy tissue. A limitation of this study is that we did
741 not evaluate the epigenomic profiles in a disease state across vascular sites. However,
742 by isolating and culturing primary adventitial fibroblasts and evaluating differential
743 response to TGFβ, we gained further insight into this mechanism. We anticipate that
744 there are dynamic changes in chromatin accessibility and gene expression programs in
745 disease, as has been previously observed[22,23], and future studies will be aimed at
746 understanding how these dynamic chromatin accessibility changes occur across
747 vascular sites. Similarly, recent work has demonstrated changes in chromatin
748 accessibility in vascular tissue with aging[81]. Our study selected for adult mice that are
749 14-16 weeks of age, which represents a young adult. We anticipate that chromatin
750 accessibility dynamically changes with aging and future studies to evaluate how this
751 change differs across vascular sites may be particularly insightful.

752

753 **Conclusions**

754 By performing combined scRNAseq and scATACseq on vascular tissue across
755 three vascular sites, we reveal for the first time that the epigenomic landscape and
756 transcriptional profiles of vascular smooth muscle, fibroblasts, and endothelial cells, are
757 specific to anatomic origin, that genomic regions and genes that differentiate cells by
758 vascular site are weighted towards developmental genes, and that vascular cells have
759 an epigenetic ‘memory’ of their developmental program. We discovered that differential
760 chromatin accessibility appears to ‘prime’ vascular site-specific gene regulatory

761 networks in disease relevant mechanisms, and finally, that genetic variants that
762 influence aortic dimension appear to regulate chromatin accessibility in not only a cell
763 type, but vascular site-specific mechanism. This work supports the paradigm that
764 genetic mechanisms of disease influence disease risk in a vascular site-specific
765 manner, gives unique insight into vascular site-specific transcriptional and epigenetic
766 programs, and further creates a valuable single cell atlas for the vascular biology
767 community.
768

769 **Methods**

770 **Data Availability**

771 All scRNAseq, scATACseq, and bulk RNAseq data has been deposited to the
772 National Center for Biotechnology Information Gene Expression Omnibus under GEO
773 accession numbers GSE296197 (scRNA/ATACseq) and GSE296074 (bulk RNAseq).
774

775 **Mice and Micro-Dissections**

776 Male 14-16-week-old C57Bl/6 mice were purchased from Jackson Laboratory
777 (Bar Harbor, ME). The animal study protocol was approved by the Administrative Panel
778 on Laboratory Animal Care at Stanford University and procedures were followed in
779 accordance with institutional guidelines.

780 Mice were anesthetized with isoflurane and sacrificed with cervical dislocation
781 technique. Vascular tissue was flushed with injection of 5mL of phosphate buffered
782 saline (PBS) into the left ventricle after an incision was made at the right atrium. Aortic
783 tissue was dissected including the aortic root and ascending aorta up to the take-off of

784 the brachiocephalic artery. The brachiocephalic artery and its extension into the right
785 common carotid artery were carefully dissected under stereoscope. The descending
786 thoracic aorta was then isolated from past the left subclavian artery down to the renal
787 arteries.
788
789 **Vascular Tissue Dissociation, Cell Capture, and Sequencing**
790 Tissues were collected and dissociated for single cell capture as previously
791 described[22,31,32]. Briefly, vascular tissue was washed three times in PBS, tissues were
792 then placed into an enzymatic dissociation cocktail (2 U ml−1 Liberase (5401127001;
793 Sigma–Aldrich) and 2 U ml−1 elastase (LS002279; Worthington) in Hank's Balanced
794 Salt Solution (HBSS)) for 45min at 37 °C. Tissues were then gently minced and
795 dissociated with pipette. The cell suspension was strained and then pelleted by
796 centrifugation at 500g for 5 min. The enzyme solution was then discarded, and cells
797 were resuspended in fresh HBSS. To increase biological replication, two sets of 8 mice
798 (16 mice total) were used to obtain two single-cell suspensions for each vascular tissue
799 (aortic root/ascending aorta, brachiocephalic/carotid, and descending thoracic aorta).
800 Cells were FACS sorted and live cells were identified as previously described[32]. Cells
801 were sorted on a Sony SH800S cell sorter, where cells were gated on forward/side
802 scatter parameters to exclude small debris and then gated on forward scatter height
803 versus forward scatter area to exclude obvious doublet events. Approximately 100-
804 150,000 live cells were sorted for each vascular site for each capture, where a portion of
805 cells were taken directly to scRNAseq capture. For single cell ATAC, cells were

806 collected in BSA-coated tubes, and nuclei isolated per 10X recommended protocol, and
807 captured on the 10X scATAC platform.
808 All single-cell capture and library preparation was performed in the Quertermous
809 Lab. Cells were loaded into a 10x Genomics microfluidics chip and encapsulated with
810 barcoded oligo-dT-containing gel beads using the 10x Genomics Chromium controller
811 according to the manufacturer's instructions. Single-cell libraries were then constructed
812 according to the manufacturer's instructions (Illumina). Libraries from individual samples
813 were multiplexed into one lane before sequencing on an Illumina platform with targeted
814 depth of 50,000 reads per cell for RNA and 75,000 reads/cell for ATAC. Sequencing
815 was performed by MedGenome (Foster City, CA). Post filtering for non-cells, mean
816 number of reads within peaks per cell in scATAC data was 18,000-20,000 as was seen
817 in our prior report[22].
818
819 **Analysis of Single-Cell Sequencing Data**
820 ***scRNAseq***
821 Fastq files from each vascular site (6 total RNA captures) were aligned to the
822 reference genome (mm10) individually using CellRanger Software (10x Genomics).
823 Dataset was then analyzed and captures were integrated using the R package Seurat[33].
824 The dataset was trimmed of cells expressing fewer than 1000 genes, and genes
825 expressed in fewer than 50 cells. The number of genes, number of unique molecular
826 identifiers and percentage of mitochondrial genes were examined to identify outliers. As
827 an unusually high number of genes can result from a 'doublet' event, in which two
828 different cell types are captured together with the same barcoded bead, cells with >7500

829 genes were discarded. Cells containing >7.5% mitochondrial genes were presumed to
830 be of poor quality and were also discarded. QC of nFeature_RNA, nCount_RNA, and
831 percent.mt are included in **Figure S6A-C**. The gene expression values then underwent
832 library-size normalization and normalized using established Single-Cell Transform
833 function in Seurat. Principal component analysis was used for dimensionality reduction,
834 followed by clustering in principal component analysis space using a graph-based
835 clustering approach via Louvain algorithm. Batch correction was performed with
836 reciprocal PCA (RPCA). UMAP was then used for two-dimensional visualization of the
837 resulting clusters. Analysis, visualization and quantification of gene expression and
838 generation of gene module scores were performed using Seurat's built-in function such
839 as "FeaturePlot", "VlnPlot", and "FindMarker."
840
841 ***scATACseq***
842 Fastq files from each vascular site (6 total ATAC captures) were aligned to the
843 reference ATAC genome (mm10) individually using CellRanger Software (10x
844 Genomics). Individual datasets were aggregated and peak calling was performed using
845 the CellRanger aggr command without subsampling normalization. The aggregated
846 dataset was then analyzed using the R package Signac[33]. The dataset was first trimmed
847 of cells containing fewer than 1000 peaks, and peaks found in fewer than 10 cells. The
848 subsequent cells were then again filtered based off TSS enrichment, nucleosome
849 signal, and percent of reads that lies within peaks found within the larger dataset. Cells
850 with greater than 20,000 reads within peaks or fewer than 3000 peaks, <2 transcription
851 start site (TSS) enrichment, or <15% reads within peaks were removed as they are

852 likely poor-quality nuclei. QC of pct_reads_in_peaks, peak_region_fragments,
853 TSS.enrichment, and nucleosome_signal are included in **Figure S6D-G**. Fragment
854 histograms based on high and low nucleosome group (NS >4, NS <4) and TSS Plot
855 based on high and low TSS enrichment (TSS >2, TSS <2) are included in **Figure**
856 **S6H&I**. The remaining cells were then processed using RunTFIDF(), RunSVD()
857 functions from Signac to allow for latent semantic indexing (LSI) of the peaks[82,83], which
858 was then used to create UMAPs. Batch correction for UMAP visualization was
859 performed with Harmony. Differentially accessible peaks between different populations
860 of cells were found using FindMarker function, using number of peaks as latent variable
861 to correct for depth. Motif matrix was obtained from JASPAR 2020, aligned onto
862 BSgenome.Mmusculus.UCSC.mm10. Accessibility analysis around transcription factor
863 motifs was performed using ChromVar[35]. Merging of scRNA and ATAC data was
864 performed using Pseudo-expression of each gene created using scATACseq
865 GeneActivity function to assign peaks to nearest genes expressed in the scRNA
866 dataset, and mapped onto each other using Canonical Correlation Analysis. For gene
867 regulatory network (GRN) analysis, RNA and ATAC integrated datasets were
868 subsampled based on cell type and GRNs were inferred using Pando[61]. In this method,
869 variable features are identified from RNA dataset and GRN is initiated with
870 'initiate_grn()' function. Candidate regions for TF binding motifs are identified and GRNs
871 are inferred using 'infer_grn()' function. GRN modules are then identified using
872 'find_modules()' function for each cell type and vascular site reported. Network graphs
873 are then visualized using 'plot_network_graph()' function and further analysis was
874 performed following standard Pando workflow.

875

876 ***ChromBPNet***

877 ***Processing of single-cell ATAC-seq data***

878 Methods for ChromBPNet model has been recently described in detail[63,84]. For
879 each cell type and vascular site cluster (i.e. SMC/Fibro/Endo, Asc/Car/Desc) from the
880 dataset, we created pooled all of the fragments that belonged to each cluster based on
881 barcode to cell type maps to create pseudobulk fragment files. We then splitting each
882 fragment in half to obtain one read per strand and converted each fragment file to a
883 tagalign file. We then used these files as input to the ENCODE ATAC-seq pipeline
884 v1.10.0 (available at https://github.com/ENCODE-DCC/atac-seq-pipeline), which
885 generated peak calls using MACS2 (available at https://github.com/macs3-
886 project/MACS). For downstream analyses involving ChromBPNet, we used the overlap
887 peak set, which only includes peaks called from the original sample that overlap with
888 peak calls from both of the pseudo-replicates created by the pipeline by randomly
889 allocating the reads from the original sample into each synthetic replicate.

890 ***Training ChromBPNet models***

891 To model the cell type and vascular–specific chromatin accessibility in each
892 vascular bed cell type, we trained ChromBPNet models on their cell type–resolved
893 pseudobulk ATAC-seq profiles (ChromBPNet is available at
894 https://github.com/kundajelab/ChromBPNet). For each sample, we used as input the
895 peak and tagalign files generated by the ENCODE ATAC-seq pipeline, along with a
896 Tn5-bias model trained on the descending aorta SMC. We trained the ChromBPNet
897 models using a 5-fold cross-validation scheme — ensuring that each chromosome

898 appeared in the test set of at least one cross-validation fold. **Table S25** outlines the
899 chromosomes included in the train, validation, and test splits for each fold in mouse.
900 Upon completion of training, any model that continued to respond to the tn5
901 motif's consensus sequences after unplugging the bias model, indicating an
902 unsuccessful bias-correction procedure, was re-trained until the model showed a limited
903 response to the tn5 motif's consensus sequences embedded in random genomic
904 backgrounds. Specifically, this retraining was performed if the maximum prediction from
905 the profile head for any base-pair from the examples containing the tn5 motif exceeded
906 0.002.

907 ***Creating the Variant List***

908 To create a comprehensive set of variants associated with aorta diameter, we
909 first obtained all of the genome-wide significant GWAS variants from Pirruccello et al.[17]
910 (p-value < 5e-8). Next, we used Plink v1.9 to find all variants from the AFR, AMR, EAS,
911 EUR, and SAS populations in 1000 genomes that are in high LD (r2 > 0.8) with the
912 genome-wide significant GWAS variants, and we used TopLD to do the same for the
913 African, East Asian, European, and South Asian populations in TOPMed. The final
914 variant list included all of the genome-wide significant variants and any variants in high
915 LD with them from any of the above populations in either 1000 genomes or TOPMed.

916 ***Predicting variant effects using ChromBPNet models***

917 To score each variant in this study, we used the ChromBPNet models for each
918 cell type to predict the base-resolution scATAC-seq coverage profiles for the 1 kb
919 genomic sequence centered at each variant and containing the reference and alternate
920 allele. We then estimated the variant's effect size using two measures: (1) the log2 fold

921 change in total predicted coverage (total counts) within each 1 kb window for the
922 alternate versus reference allele and (2) the Jensen–Shannon distance (JSD) between
923 the base-resolution predicted probability profiles for the reference and alternate allele
924 (capturing changes in profile shape).

925 We assessed statistical significance for these scores using empirical null distributions
926 constructed by shuffling the 2114 bp sequence around each variant multiple times while
927 preserving dinucleotide frequency. Next, each shuffled sequence was duplicated, and
928 the variant's reference or alternate allele was inserted at the center, resulting in a total
929 of one million null variants for each set of observed variants scored. Each null variant
930 was scored with the same procedure as the observed variants. For each observed
931 variant, we then computed the proportion of null variants with an equally high or higher
932 (more extreme) score to derive empirical *P*-values for the log2 fold change and JSD
933 scores. The code base for scoring variants is at https://github.com/kundajelab/variant-
934 scorer.

935 ***Motif enrichment analysis from scored ChromBPNet variants***

936 To identify variants that have differential effect based on vascular site (i.e.
937 between ascending and descending aortic cell types), we performed linear regression
938 analysis for absolute log fold change between all scored variants between ascending
939 and descending SMC, fibroblasts, and endothelial cell ChromBPNet models. We
940 identified the top 1% of variants that 'deviate' from the linear regression line that
941 represent the top 1% of variants that have a differing effect based on vascular site
942 within cell type. The genomic position of this top 1% variant list was expanded 100bp
943 upstream and downstream to have a 200bp window that was converted to a BED file.

944 These genomic positions were then used unbiased Motif Discovery function with MEME
945 Suite[64]. Known motif analysis of top discovered motifs was then performed using
946 TOMTOM (HOCOMOCOv11)[65].
947
948 **Primary adventitial fibroblast culture and bulk RNA sequencing**
949 We isolated the aortic root and ascending aorta from 6, 12-week-old male
950 C57/BL6 mice as well as the descending thoracic aorta to the level of the renal arteries
951 and carefully separated the media from the adventitia by gentle traction with forceps.
952 Adventitia was cut into small pieces with microscissors and plated into 12 well plates
953 with DMEM media with 5% FBS. Following cell attachment to the plate, cells were
954 cultured at 37C and expanded for 48 hours. Cells were washed with PBS and passaged
955 1x and plated into a 12 well plate at 65,000 cells/mL. Upon cell culture reaching ~80%
956 confluence, cells were treated with either solute control or mouse TGFβ (invitae)
957 (10ng/mL) for 48 hours. Following 48hr treatment, RNA was isolated using Qiagen
958 RNeasy kits and RNA/cDNA library was sequenced with 250M paired end reads. Fastq
959 files were aligned to MM10 murine genome and raw read count and expression
960 normalization was performed with featureCounts[85] and DEseq2[86], respectively. Using
961 DEseq2 standard pipeline, we performed differential gene expression analysis between
962 groups (i.e. Asc-control versus Desc-control; Asc-TGFβ versus Desc-TGFβ; Asc-control
963 versus Asc-TGFβ; Desc-control versus Desc-TGFβ). Further interaction analysis was
964 performed where DESeq2 pipeline evaluates genes whose response to TGFβ is not the
965 same in both regions — genes that are regulated by TGFβ in one aortic region but not
966 the other, or that change in opposite directions, helping identify region-specific

967 responses to TGFβ. Differential predicted transcription factor motif accessibility from
968 bulk RNAseq analysis of the 200bp upstream of the transcription start site (TSS) from
969 differentially expressed genes was performed with Hypergeometric Optimization of Motif
970 EnRichment (HOMER)[62].
971

972 **Acknowledgements**

973 **Funding:**
974
975 National Institutes of Health grant F32HL160067 (CW)
976 National Institutes of Health grant L30HL159413 (CW)
977 National Institutes of Health grant K08HL167699 (CW)
978 National Institutes of Health grant K08HL153798 (PC)
979 National Institutes of Health grant R01HL134817 (TQ)
980 National Institutes of Health grant R01HL139478 (TQ)
981 National Institutes of Health grant R01HL156846 (TQ)
982 National Institutes of Health grant R01HL151535 (TQ)
983 National Institutes of Health grant R01HL145708 (TQ)
984 National Institutes of Health grant UM1 HG011972 (TQ)
985 American Heart Association grant 20CDA35310303 (PC)
986 American Heart Association grant 23CDA1042900 (CW)
987 American Heart Association grant 23POST1018991 (WG).
988

989 **Disclosures**

990 TQ is a scientific advisor for Amgen. CSW is a consultant and advisory board member
991 for Avidity Biosciences and AIRNA bio. All other authors have no disclosures.
992

993 **References**
994

995 1. Haimovici H, Maier N. Fate of Aortic Homografts in Canine Atherosclerosis. 3.
996 Study of Fresh Abdominal and Thoracic Aortic Implants into Thoracic Aorta: Role
997 of Tissue Susceptibility in Atherogenesis. *Arch Surg*. 1964;89:961-969. doi:
998 10.1001/archsurg.1964.01320060029006
999 2. Haimovici H, Maier N, Strauss L. Fate of aortic homografts in experimental
1000 canine atherosclerosis; study of fresh thoracic implants into abdominal aorta.
1001 *AMA Arch Surg*. 1958;76:282-288. doi: 10.1001/archsurg.1958.01280200104012

1002 3. Haimovici H, Maier N, Strauss L. Fate of aortic homografts in experimental
1003 canine atherosclerosis. II. Study of fresh abdominal aortic implants into
1004 abdominal aorta. *AMA Arch Surg*. 1959;78:239-245. doi:
1005 10.1001/archsurg.1959.04320020061010
1006 4. Katz TC, Singh MK, Degenhardt K, Rivera-Feliciano J, Johnson RL, Epstein JA,
1007 Tabin CJ. Distinct compartments of the proepicardial organ give rise to coronary
1008 vascular endothelial cells. *Dev Cell*. 2012;22:639-650. doi:
1009 10.1016/j.devcel.2012.01.012
1010 5. Majesky MW. Developmental basis of vascular smooth muscle diversity.
1011 *Arterioscler Thromb Vasc Biol*. 2007;27:1248-1258. doi:
1012 10.1161/ATVBAHA.107.141069
1013 6. Mikawa T, Gourdie RG. Pericardial mesoderm generates a population of
1014 coronary smooth muscle cells migrating into the heart along with ingrowth of the
1015 epicardial organ. *Dev Biol*. 1996;174:221-232. doi: 10.1006/dbio.1996.0068
1016 7. Red-Horse K, Ueno H, Weissman IL, Krasnow MA. Coronary arteries form by
1017 developmental reprogramming of venous cells. *Nature*. 2010;464:549-553. doi:
1018 10.1038/nature08873
1019 8. Sawada H, Rateri DL, Moorleghen JJ, Majesky MW, Daugherty A. Smooth
1020 Muscle Cells Derived From Second Heart Field and Cardiac Neural Crest Reside
1021 in Spatially Distinct Domains in the Media of the Ascending Aorta-Brief Report.
1022 *Arterioscler Thromb Vasc Biol*. 2017;37:1722-1726. doi:
1023 10.1161/ATVBAHA.117.309599
1024 9. Tian X, Hu T, Zhang H, He L, Huang X, Liu Q, Yu W, He L, Yang Z, Zhang Z, et
1025 al. Subepicardial endothelial cells invade the embryonic ventricle wall to form
1026 coronary arteries. *Cell Res*. 2013;23:1075-1090. doi: 10.1038/cr.2013.83
1027 10. Volz KS, Jacobs AH, Chen HI, Poduri A, McKay AS, Riordan DP, Kofler N,
1028 Kitajewski J, Weissman I, Red-Horse K. Pericytes are progenitors for coronary
1029 artery smooth muscle. *Elife*. 2015;4. doi: 10.7554/eLife.10036
1030 11. Jones GT, Tromp G, Kuivaniemi H, Gretarsdottir S, Baas AF, Giusti B, Strauss E,
1031 Van't Hof FN, Webb TR, Erdman R, et al. Meta-Analysis of Genome-Wide
1032 Association Studies for Abdominal Aortic Aneurysm Identifies Four New Disease-
1033 Specific Risk Loci. *Circ Res*. 2017;120:341-353. doi:
1034 10.1161/CIRCRESAHA.116.308765
1035 12. Nikpay M, Goel A, Won HH, Hall LM, Willenborg C, Kanoni S, Saleheen D,
1036 Kyriakou T, Nelson CP, Hopewell JC, et al. A comprehensive 1,000 Genomes-
1037 based genome-wide association meta-analysis of coronary artery disease. *Nat*
1038 *Genet*. 2015;47:1121-1130. doi: 10.1038/ng.3396
1039 13. Schunkert H, Konig IR, Kathiresan S, Reilly MP, Assimes TL, Holm H, Preuss M,
1040 Stewart AF, Barbalic M, Gieger C, et al. Large-scale association analysis
1041 identifies 13 new susceptibility loci for coronary artery disease. *Nat Genet*.
1042 2011;43:333-338. doi: 10.1038/ng.784
1043 14. van der Harst P, Verweij N. Identification of 64 Novel Genetic Loci Provides an
1044 Expanded View on the Genetic Architecture of Coronary Artery Disease. *Circ*
1045 *Res*. 2018;122:433-443. doi: 10.1161/CIRCRESAHA.117.312086
1046 15. Strawbridge RJ, Ward J, Bailey MES, Cullen B, Ferguson A, Graham N,
1047 Johnston KJA, Lyall LM, Pearsall R, Pell J, et al. Carotid Intima-Media Thickness:

1048 Novel Loci, Sex-Specific Effects, and Genetic Correlations With Obesity and
1049 Glucometabolic Traits in UK Biobank. *Arterioscler Thromb Vasc Biol*.
1050 2020;40:446-461. doi: 10.1161/ATVBAHA.119.313226
1051 16. Franceschini N, Giambartolomei C, de Vries PS, Finan C, Bis JC, Huntley RP,
1052 Lovering RC, Tajuddin SM, Winkler TW, Graff M, et al. GWAS and colocalization
1053 analyses implicate carotid intima-media thickness and carotid plaque loci in
1054 cardiovascular outcomes. *Nat Commun*. 2018;9:5141. doi: 10.1038/s41467-018-
1055 07340-5
1056 17. Pirruccello JP, Chaffin MD, Chou EL, Fleming SJ, Lin H, Nekoui M, Khurshid S,
1057 Friedman SF, Bick AG, Arduini A, et al. Deep learning enables genetic analysis
1058 of the human thoracic aorta. *Nat Genet*. 2022;54:40-51. doi: 10.1038/s41588-
1059 021-00962-4
1060 18. Oudelaar AM, Higgs DR. The relationship between genome structure and
1061 function. *Nat Rev Genet*. 2021;22:154-168. doi: 10.1038/s41576-020-00303-x
1062 19. Anene-Nzelu CG, Lee MCJ, Tan WLW, Dashi A, Foo RSY. Genomic enhancers
1063 in cardiac development and disease. *Nat Rev Cardiol*. 2022;19:7-25. doi:
1064 10.1038/s41569-021-00597-2
1065 20. Alexanian M, Przytycki PF, Micheletti R, Padmanabhan A, Ye L, Travers JG,
1066 Gonzalez-Teran B, Silva AC, Duan Q, Ranade SS, et al. A transcriptional switch
1067 governs fibroblast activation in heart disease. *Nature*. 2021;595:438-443. doi:
1068 10.1038/s41586-021-03674-1
1069 21. Hocker JD, Poirion OB, Zhu F, Buchanan J, Zhang K, Chiou J, Wang TM, Zhang
1070 Q, Hou X, Li YE, et al. Cardiac cell type-specific gene regulatory programs and
1071 disease risk association. *Sci Adv*. 2021;7. doi: 10.1126/sciadv.abf1444
1072 22. Cheng P, Wirka RC, Clarke LS, Zhao Q, Kundu R, Nguyen T, Nair S, Sharma D,
1073 Kim HJ, Shi H, et al. ZEB2 Shapes the Epigenetic Landscape of Atherosclerosis.
1074 *Circulation*. 2022. doi: 10.1161/CIRCULATIONAHA.121.057789
1075 23. Wang Y, Gao H, Wang F, Ye Z, Mokry M, Turner AW, Ye J, Koplev S, Luo L,
1076 Alsaigh T, et al. Dynamic changes in chromatin accessibility are associated with
1077 the atherogenic transitioning of vascular smooth muscle cells. *Cardiovasc Res*.
1078 2021. doi: 10.1093/cvr/cvab347
1079 24. Depuydt MAC, Prange KHM, Slenders L, Ord T, Elbersen D, Boltjes A, de Jager
1080 SCA, Asselbergs FW, de Borst GJ, Aavik E, et al. Microanatomy of the Human
1081 Atherosclerotic Plaque by Single-Cell Transcriptomics. *Circ Res*. 2020;127:1437-
1082 1455. doi: 10.1161/CIRCRESAHA.120.316770
1083 25. Aquino JB, Sierra R, Montaldo LA. Diverse cellular origins of adult blood vascular
1084 endothelial cells. *Dev Biol*. 2021;477:117-132. doi: 10.1016/j.ydbio.2021.05.010
1085 26. Anderson MJ, Pham VN, Vogel AM, Weinstein BM, Roman BL. Loss of unc45a
1086 precipitates arteriovenous shunting in the aortic arches. *Dev Biol*. 2008;318:258-
1087 267. doi: 10.1016/j.ydbio.2008.03.022
1088 27. Li P, Pashmforoush M, Sucov HM. Mesodermal retinoic acid signaling regulates
1089 endothelial cell coalescence in caudal pharyngeal arch artery vasculogenesis.
1090 *Dev Biol*. 2012;361:116-124. doi: 10.1016/j.ydbio.2011.10.018
1091 28. Paffett-Lugassy N, Singh R, Nevis KR, Guner-Ataman B, O'Loughlin E, Jahangiri
1092 L, Harvey RP, Burns CG, Burns CE. Heart field origin of great vessel precursors

1093 relies on nkx2.5-mediated vasculogenesis. *Nat Cell Biol*. 2013;15:1362-1369.
1094 doi: 10.1038/ncb2862
1095 29. Dobnikar L, Taylor AL, Chappell J, Oldach P, Harman JL, Oerton E, Dzierzak E,
1096 Bennett MR, Spivakov M, Jorgensen HF. Disease-relevant transcriptional
1097 signatures identified in individual smooth muscle cells from healthy mouse
1098 vessels. *Nat Commun*. 2018;9:4567. doi: 10.1038/s41467-018-06891-x
1099 30. Yu L, Zhang J, Gao A, Zhang M, Wang Z, Yu F, Guo X, Su G, Zhang Y, Zhang
1100 M, et al. An intersegmental single-cell profile reveals aortic heterogeneity and
1101 identifies a novel Malat1(+) vascular smooth muscle subtype involved in
1102 abdominal aortic aneurysm formation. *Signal Transduct Target Ther*. 2022;7:125.
1103 doi: 10.1038/s41392-022-00943-x
1104 31. Kim JB, Zhao Q, Nguyen T, Pjanic M, Cheng P, Wirka R, Travisano S, Nagao M,
1105 Kundu R, Quertermous T. Environment-Sensing Aryl Hydrocarbon Receptor
1106 Inhibits the Chondrogenic Fate of Modulated Smooth Muscle Cells in
1107 Atherosclerotic Lesions. *Circulation*. 2020;142:575-590. doi:
1108 10.1161/CIRCULATIONAHA.120.045981
1109 32. Wirka RC, Wagh D, Paik DT, Pjanic M, Nguyen T, Miller CL, Kundu R, Nagao M,
1110 Coller J, Koyano TK, et al. Atheroprotective roles of smooth muscle cell
1111 phenotypic modulation and the TCF21 disease gene as revealed by single-cell
1112 analysis. *Nat Med*. 2019;25:1280-1289. doi: 10.1038/s41591-019-0512-5
1113 33. Stuart T, Butler A, Hoffman P, Hafemeister C, Papalexi E, Mauck WM, 3rd, Hao
1114 Y, Stoeckius M, Smibert P, Satija R. Comprehensive Integration of Single-Cell
1115 Data. *Cell*. 2019;177:1888-1902 e1821. doi: 10.1016/j.cell.2019.05.031
1116 34. McLean CY, Bristor D, Hiller M, Clarke SL, Schaar BT, Lowe CB, Wenger AM,
1117 Bejerano G. GREAT improves functional interpretation of cis-regulatory regions.
1118 *Nat Biotechnol*. 2010;28:495-501. doi: 10.1038/nbt.1630
1119 35. Schep AN, Wu B, Buenrostro JD, Greenleaf WJ. chromVAR: inferring
1120 transcription-factor-associated accessibility from single-cell epigenomic data. *Nat*
1121 *Methods*. 2017;14:975-978. doi: 10.1038/nmeth.4401
1122 36. Liu J, Ren Y, Kang L, Zhang L. Overexpression of CCN3 inhibits inflammation
1123 and progression of atherosclerosis in apolipoprotein E-deficient mice. *PLoS One*.
1124 2014;9:e94912. doi: 10.1371/journal.pone.0094912
1125 37. Shimoyama T, Hiraoka S, Takemoto M, Koshizaka M, Tokuyama H, Tokuyama
1126 T, Watanabe A, Fujimoto M, Kawamura H, Sato S, et al. CCN3 inhibits
1127 neointimal hyperplasia through modulation of smooth muscle cell growth and
1128 migration. *Arterioscler Thromb Vasc Biol*. 2010;30:675-682. doi:
1129 10.1161/ATVBAHA.110.203356
1130 38. Al Haj Zen A, Caligiuri G, Sainz J, Lemitre M, Demerens C, Lafont A. Decorin
1131 overexpression reduces atherosclerosis development in apolipoprotein E-
1132 deficient mice. *Atherosclerosis*. 2006;187:31-39. doi:
1133 10.1016/j.atherosclerosis.2005.08.023
1134 39. Licht AH, Nubel T, Feldner A, Jurisch-Yaksi N, Marcello M, Demicheva E, Hu JH,
1135 Hartenstein B, Augustin HG, Hecker M, et al. Junb regulates arterial contraction
1136 capacity, cellular contractility, and motility via its target Myl9 in mice. *J Clin*
1137 *Invest*. 2010;120:2307-2318. doi: 10.1172/JCI41749

1138 40. Yoshida T, Kaestner KH, Owens GK. Conditional deletion of Kruppel-like factor 4
1139 delays downregulation of smooth muscle cell differentiation markers but
1140 accelerates neointimal formation following vascular injury. *Circ Res*.
1141 2008;102:1548-1557. doi: 10.1161/CIRCRESAHA.108.176974
1142 41. Li J, Adams LD, Wang X, Pabon L, Schwartz SM, Sane DC, Geary RL. Regulator
1143 of G protein signaling 5 marks peripheral arterial smooth muscle cells and is
1144 downregulated in atherosclerotic plaque. *J Vasc Surg*. 2004;40:519-528. doi:
1145 10.1016/j.jvs.2004.06.021
1146 42. Daniel JM, Prock A, Dutzmann J, Sonnenschein K, Thum T, Bauersachs J,
1147 Sedding DG. Regulator of G-Protein Signaling 5 Prevents Smooth Muscle Cell
1148 Proliferation and Attenuates Neointima Formation. *Arterioscler Thromb Vasc Biol*.
1149 2016;36:317-327. doi: 10.1161/ATVBAHA.115.305974
1150 43. Paloschi V, Kurtovic S, Folkersen L, Gomez D, Wagsater D, Roy J, Petrini J,
1151 Eriksson MJ, Caidahl K, Hamsten A, et al. Impaired splicing of fibronectin is
1152 associated with thoracic aortic aneurysm formation in patients with bicuspid
1153 aortic valve. *Arterioscler Thromb Vasc Biol*. 2011;31:691-697. doi:
1154 10.1161/ATVBAHA.110.218461
1155 44. Soubeyrand S, Lau P, Nikpay M, Dang AT, McPherson R. Common
1156 Polymorphism That Protects From Cardiovascular Disease Increases Fibronectin
1157 Processing and Secretion. *Circ Genom Precis Med*. 2022:CIRCGEN121003428.
1158 doi: 10.1161/CIRCGEN.121.003428
1159 45. Azad AK, Chakrabarti S, Xu Z, Davidge ST, Fu Y. Coiled-coil domain containing
1160 3 (CCDC3) represses tumor necrosis factor-alpha/nuclear factor kappaB-induced
1161 endothelial inflammation. *Cell Signal*. 2014;26:2793-2800. doi:
1162 10.1016/j.cellsig.2014.08.025
1163 46. van de Laar IM, Oldenburg RA, Pals G, Roos-Hesselink JW, de Graaf BM,
1164 Verhagen JM, Hoedemaekers YM, Willemsen R, Severijnen LA, Venselaar H, et
1165 al. Mutations in SMAD3 cause a syndromic form of aortic aneurysms and
1166 dissections with early-onset osteoarthritis. *Nat Genet*. 2011;43:121-126. doi:
1167 10.1038/ng.744
1168 47. Iyer D, Zhao Q, Wirka R, Naravane A, Nguyen T, Liu B, Nagao M, Cheng P,
1169 Miller CL, Kim JB, et al. Coronary artery disease genes SMAD3 and TCF21
1170 promote opposing interactive genetic programs that regulate smooth muscle cell
1171 differentiation and disease risk. *PLoS Genet*. 2018;14:e1007681. doi:
1172 10.1371/journal.pgen.1007681
1173 48. Renard M, Francis C, Ghosh R, Scott AF, Witmer PD, Ades LC, Andelfinger GU,
1174 Arnaud P, Boileau C, Callewaert BL, et al. Clinical Validity of Genes for Heritable
1175 Thoracic Aortic Aneurysm and Dissection. *J Am Coll Cardiol*. 2018;72:605-615.
1176 doi: 10.1016/j.jacc.2018.04.089
1177 49. Chou E, Pirruccello JP, Ellinor PT, Lindsay ME. Genetics and mechanisms of
1178 thoracic aortic disease. *Nat Rev Cardiol*. 2023;20:168-180. doi: 10.1038/s41569-
1179 022-00763-0
1180 50. Regard JB, Scheek S, Borbiev T, Lanahan AA, Schneider A, Demetriades AM,
1181 Hiemisch H, Barnes CA, Verin AD, Worley PF. Verge: a novel vascular early
1182 response gene. *J Neurosci*. 2004;24:4092-4103. doi:
1183 10.1523/JNEUROSCI.4252-03.2004

1184 51. Diaz-Canestro C, Bonetti NR, Wust P, Nageswaran V, Liberale L, Beer JH,
1185 Montecucco F, Luscher TF, Bohacek J, Camici GG. Apold1 deficiency associates
1186 with increased arterial thrombosis in vivo. *Eur J Clin Invest*. 2020;50:e13191. doi:
1187 10.1111/eci.13191
1188 52. Briot A, Jaroszewicz A, Warren CM, Lu J, Touma M, Rudat C, Hofmann JJ, Airik
1189 R, Weinmaster G, Lyons K, et al. Repression of Sox9 by Jag1 is continuously
1190 required to suppress the default chondrogenic fate of vascular smooth muscle
1191 cells. *Dev Cell*. 2014;31:707-721. doi: 10.1016/j.devcel.2014.11.023
1192 53. Martos-Rodriguez CJ, Albarran-Juarez J, Morales-Cano D, Caballero A,
1193 MacGrogan D, de la Pompa JL, Carramolino L, Bentzon JF. Fibrous Caps in
1194 Atherosclerosis Form by Notch-Dependent Mechanisms Common to Arterial
1195 Media Development. *Arterioscler Thromb Vasc Biol*. 2021;41:e427-e439. doi:
1196 10.1161/ATVBAHA.120.315627
1197 54. Hubner K, Grassme KS, Rao J, Wenke NK, Zimmer CL, Korte L, Muller K,
1198 Sumanas S, Greber B, Herzog W. Wnt signaling positively regulates endothelial
1199 cell fate specification in the Fli1a-positive progenitor population via Lef1. *Dev*
1200 *Biol*. 2017;430:142-155. doi: 10.1016/j.ydbio.2017.08.004
1201 55. Oettgen P. Regulation of vascular inflammation and remodeling by ETS factors.
1202 *Circ Res*. 2006;99:1159-1166. doi: 10.1161/01.RES.0000251056.85990.db
1203 56. Schafer CM, Gurley JM, Kurylowicz K, Lin PK, Chen W, Elliott MH, Davis GE,
1204 Bhatti F, Griffin CT. An inhibitor of endothelial ETS transcription factors promotes
1205 physiologic and therapeutic vessel regression. *Proc Natl Acad Sci U S A*.
1206 2020;117:26494-26502. doi: 10.1073/pnas.2015980117
1207 57. Mukherjee K, Pingili AK, Singh P, Dhodi AN, Dutta SR, Gonzalez FJ, Malik KU.
1208 Testosterone Metabolite 6beta-Hydroxytestosterone Contributes to Angiotensin
1209 II-Induced Abdominal Aortic Aneurysms in Apoe(-/-) Male Mice. *J Am Heart*
1210 *Assoc*. 2021;10:e018536. doi: 10.1161/JAHA.120.018536
1211 58. Thirunavukkarasu S, Khan NS, Song CY, Ghafoor HU, Brand DD, Gonzalez FJ,
1212 Malik KU. Cytochrome P450 1B1 Contributes to the Development of Angiotensin
1213 II-Induced Aortic Aneurysm in Male Apoe(-/-) Mice. *Am J Pathol*. 2016;186:2204-
1214 2219. doi: 10.1016/j.ajpath.2016.04.005
1215 59. Traylor M, Tozer DJ, Croall ID, Lisiecka-Ford DM, Olorunda AO, Boncoraglio G,
1216 Dichgans M, Lemmens R, Rosand J, Rost NS, et al. Genetic variation in
1217 PLEKHG1 is associated with white matter hyperintensities (n = 11,226).
1218 *Neurology*. 2019;92:e749-e757. doi: 10.1212/WNL.0000000000006952
1219 60. Zernecke A, Winkels H, Cochain C, Williams JW, Wolf D, Soehnlein O, Robbins
1220 CS, Monaco C, Park I, McNamara CA, et al. Meta-Analysis of Leukocyte
1221 Diversity in Atherosclerotic Mouse Aortas. *Circ Res*. 2020;127:402-426. doi:
1222 10.1161/CIRCRESAHA.120.316903
1223 61. Fleck JS, Jansen SMJ, Wollny D, Zenk F, Seimiya M, Jain A, Okamoto R, Santel
1224 M, He Z, Camp JG, et al. Inferring and perturbing cell fate regulomes in human
1225 brain organoids. *Nature*. 2023;621:365-372. doi: 10.1038/s41586-022-05279-8
1226 62. Heinz S, Benner C, Spann N, Bertolino E, Lin YC, Laslo P, Cheng JX, Murre C,
1227 Singh H, Glass CK. Simple combinations of lineage-determining transcription
1228 factors prime cis-regulatory elements required for macrophage and B cell
1229 identities. *Mol Cell*. 2010;38:576-589. doi: 10.1016/j.molcel.2010.05.004

1230 63. Pampari A, Shcherbina A, Kvon EZ, Kosicki M, Nair S, Kundu S, Kathiria AS,
1231 Risca VI, Kuningas K, Alasoo K, et al. ChromBPNet: bias factorized, base-
1232 resolution deep learning models of chromatin accessibility reveal cis-regulatory
1233 sequence syntax, transcription factor footprints and regulatory variants. *bioRxiv*.
1234 2025. doi: 10.1101/2024.12.25.630221
1235 64. Bailey TL, Johnson J, Grant CE, Noble WS. The MEME Suite. *Nucleic Acids*
1236 *Res*. 2015;43:W39-49. doi: 10.1093/nar/gkv416
1237 65. Gupta S, Stamatoyannopoulos JA, Bailey TL, Noble WS. Quantifying similarity
1238 between motifs. *Genome Biol*. 2007;8:R24. doi: 10.1186/gb-2007-8-2-r24
1239 66. Maurano MT, Humbert R, Rynes E, Thurman RE, Haugen E, Wang H, Reynolds
1240 AP, Sandstrom R, Qu H, Brody J, et al. Systematic localization of common
1241 disease-associated variation in regulatory DNA. *Science*. 2012;337:1190-1195.
1242 doi: 10.1126/science.1222794
1243 67. Chen Y, Xiao D, Zhang L, Cai CL, Li BY, Liu Y. The Role of Tbx20 in
1244 Cardiovascular Development and Function. *Front Cell Dev Biol*. 2021;9:638542.
1245 doi: 10.3389/fcell.2021.638542
1246 68. Koyama S, Ito K, Terao C, Akiyama M, Horikoshi M, Momozawa Y, Matsunaga
1247 H, Ieki H, Ozaki K, Onouchi Y, et al. Population-specific and trans-ancestry
1248 genome-wide analyses identify distinct and shared genetic risk loci for coronary
1249 artery disease. *Nat Genet*. 2020;52:1169-1177. doi: 10.1038/s41588-020-0705-3
1250 69. Sakaue S, Kanai M, Tanigawa Y, Karjalainen J, Kurki M, Koshiba S, Narita A,
1251 Konuma T, Yamamoto K, Akiyama M, et al. A cross-population atlas of genetic
1252 associations for 220 human phenotypes. *Nat Genet*. 2021;53:1415-1424. doi:
1253 10.1038/s41588-021-00931-x
1254 70. Warren HR, Evangelou E, Cabrera CP, Gao H, Ren M, Mifsud B, Ntalla I,
1255 Surendran P, Liu C, Cook JP, et al. Genome-wide association analysis identifies
1256 novel blood pressure loci and offers biological insights into cardiovascular risk.
1257 *Nat Genet*. 2017;49:403-415. doi: 10.1038/ng.3768
1258 71. Benjamins JW, Yeung MW, van de Vegte YJ, Said MA, van der Linden T, Ties D,
1259 Juarez-Orozco LE, Verweij N, van der Harst P. Genomic insights in ascending
1260 aortic size and distensibility. *EBioMedicine*. 2022;75:103783. doi:
1261 10.1016/j.ebiom.2021.103783
1262 72. Takeuchi F, Akiyama M, Matoba N, Katsuya T, Nakatochi M, Tabara Y, Narita A,
1263 Saw WY, Moon S, Spracklen CN, et al. Interethnic analyses of blood pressure
1264 loci in populations of East Asian and European descent. *Nat Commun*.
1265 2018;9:5052. doi: 10.1038/s41467-018-07345-0
1266 73. Kichaev G, Bhatia G, Loh PR, Gazal S, Burch K, Freund MK, Schoech A,
1267 Pasaniuc B, Price AL. Leveraging Polygenic Functional Enrichment to Improve
1268 GWAS Power. *Am J Hum Genet*. 2019;104:65-75. doi:
1269 10.1016/j.ajhg.2018.11.008
1270 74. Roselli C, Chaffin MD, Weng LC, Aeschbacher S, Ahlberg G, Albert CM, Almgren
1271 P, Alonso A, Anderson CD, Aragam KG, et al. Multi-ethnic genome-wide
1272 association study for atrial fibrillation. *Nat Genet*. 2018;50:1225-1233. doi:
1273 10.1038/s41588-018-0133-9
1274 75. Acharya A, Baek ST, Huang G, Eskiocak B, Goetsch S, Sung CY, Banfi S, Sauer
1275 MF, Olsen GS, Duffield JS, et al. The bHLH transcription factor Tcf21 is required

1276 for lineage-specific EMT of cardiac fibroblast progenitors. *Development*.
1277 2012;139:2139-2149. doi: 10.1242/dev.079970
1278 76. Fardi M, Alivand M, Baradaran B, Farshdousti Hagh M, Solali S. The crucial role
1279 of ZEB2: From development to epithelial-to-mesenchymal transition and cancer
1280 complexity. *J Cell Physiol*. 2019. doi: 10.1002/jcp.28277
1281 77. Erdmann J, Kessler T, Munoz Venegas L, Schunkert H. A decade of genome-
1282 wide association studies for coronary artery disease: the challenges ahead.
1283 *Cardiovasc Res*. 2018;114:1241-1257. doi: 10.1093/cvr/cvy084
1284 78. Gadson PF, Jr., Dalton ML, Patterson E, Svoboda DD, Hutchinson L, Schram D,
1285 Rosenquist TH. Differential response of mesoderm- and neural crest-derived
1286 smooth muscle to TGF-beta1: regulation of c-myb and alpha1 (I) procollagen
1287 genes. *Exp Cell Res*. 1997;230:169-180. doi: 10.1006/excr.1996.3398
1288 79. Topouzis S, Majesky MW. Smooth muscle lineage diversity in the chick embryo.
1289 Two types of aortic smooth muscle cell differ in growth and receptor-mediated
1290 transcriptional responses to transforming growth factor-beta. *Dev Biol*.
1291 1996;178:430-445. doi: 10.1006/dbio.1996.0229
1292 80. Forte E, Ramialison M, Nim HT, Mara M, Li JY, Cohn R, Daigle SL, Boyd S,
1293 Stanley EG, Elefanty AG, et al. Adult mouse fibroblasts retain organ-specific
1294 transcriptomic identity. *Elife*. 2022;11. doi: 10.7554/eLife.71008
1295 81. Xie W, Ke Y, You Q, Li J, Chen L, Li D, Fang J, Chen X, Zhou Y, Chen L, et al.
1296 Single-Cell RNA Sequencing and Assay for Transposase-Accessible Chromatin
1297 Using Sequencing Reveals Cellular and Molecular Dynamics of Aortic Aging in
1298 Mice. *Arterioscler Thromb Vasc Biol*. 2022;42:156-171. doi:
1299 10.1161/ATVBAHA.121.316883
1300 82. Cusanovich DA, Daza R, Adey A, Pliner HA, Christiansen L, Gunderson KL,
1301 Steemers FJ, Trapnell C, Shendure J. Multiplex single cell profiling of chromatin
1302 accessibility by combinatorial cellular indexing. *Science*. 2015;348:910-914. doi:
1303 10.1126/science.aab1601
1304 83. Cusanovich DA, Reddington JP, Garfield DA, Daza RM, Aghamirzaie D, Marco-
1305 Ferreres R, Pliner HA, Christiansen L, Qiu X, Steemers FJ, et al. The cis-
1306 regulatory dynamics of embryonic development at single-cell resolution. *Nature*.
1307 2018;555:538-542. doi: 10.1038/nature25981
1308 84. Marderstein AR, Kundu S, Padhi EM, Deshpande S, Wang A, Robb E, Sun Y,
1309 Yun CM, Pomales-Matos D, Xie Y, et al. Mapping the regulatory effects of
1310 common and rare non-coding variants across cellular and developmental
1311 contexts in the brain and heart. *bioRxiv*. 2025. doi: 10.1101/2025.02.18.638922
1312 85. Liao Y, Smyth GK, Shi W. featureCounts: an efficient general purpose program
1313 for assigning sequence reads to genomic features. *Bioinformatics*. 2014;30:923-
1314 930. doi: 10.1093/bioinformatics/btt656
1315 86. Love MI, Huber W, Anders S. Moderated estimation of fold change and
1316 dispersion for RNA-seq data with DESeq2. *Genome Biol*. 2014;15:550. doi:
1317 10.1186/s13059-014-0550-8
1318

1319

1320 **Figures and Figure Legends**

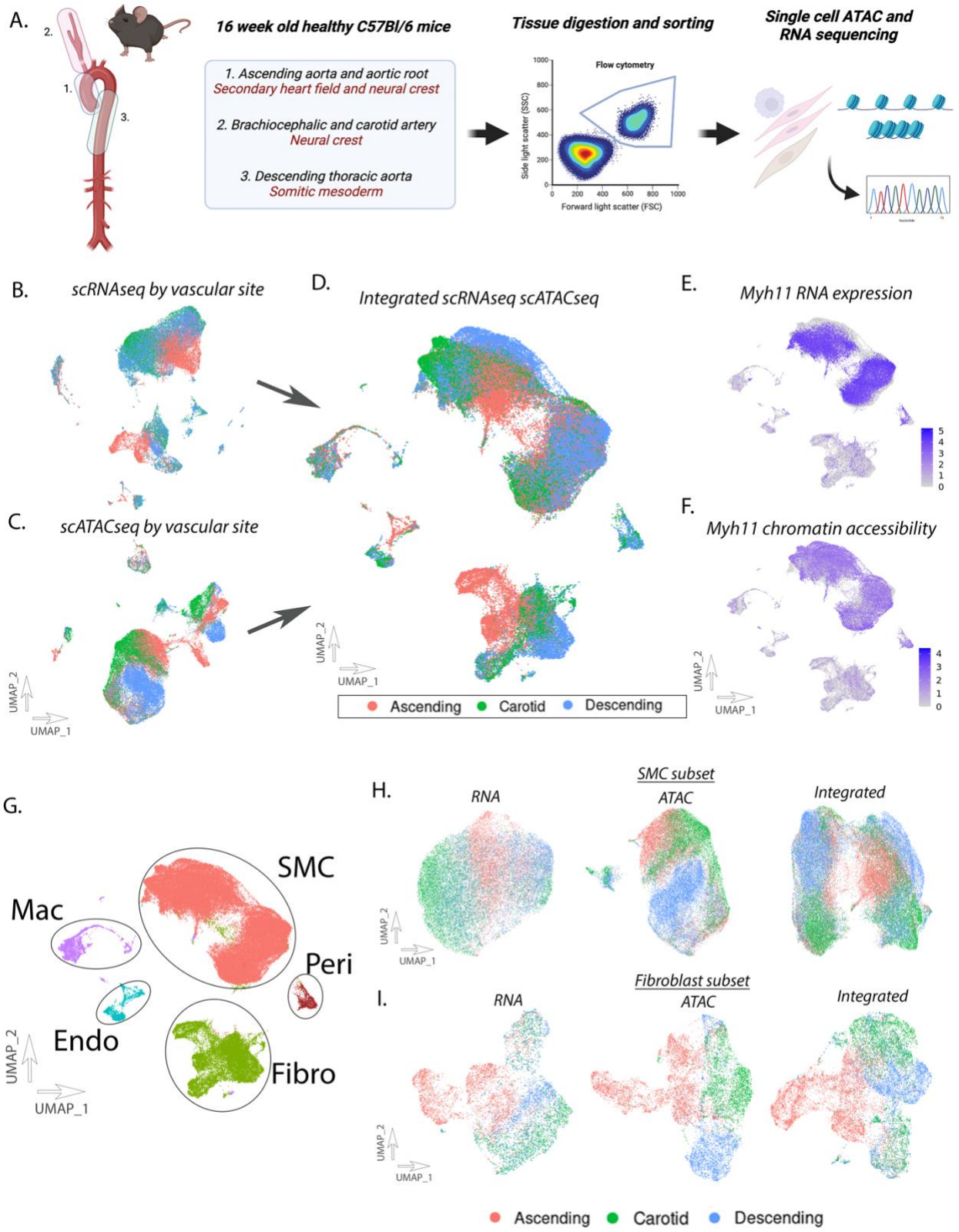

1321

1322 **Figure 1. Transcriptomic and epigenomic landscape of single vascular cells.**

1323 Single cell RNA seq (scRNAseq) and single cell ATAC seq (scATACseq) was

1324 performed on vascular tissue in adult healthy mice C57Bl/6) in three vascular sites

1325 (aortic root/ascending aorta, brachiocephalic/carotid artery, descending thoracic

1326 aorta)(A). UMAP of scRNAseq data (B), scATACseq data (C), and integrated datasets

1327 (D). RNA expression *Myh11* in integrated dataset (E). Chromatin accessibility of *Myh11*

1328 in integrated dataset (F). Differentiation of major cell populations of the vascular wall

1329 (G). Subset analysis for scRNA, scATAC, and integrated datasets in SMC (H) and

1330 Fibroblast (I).

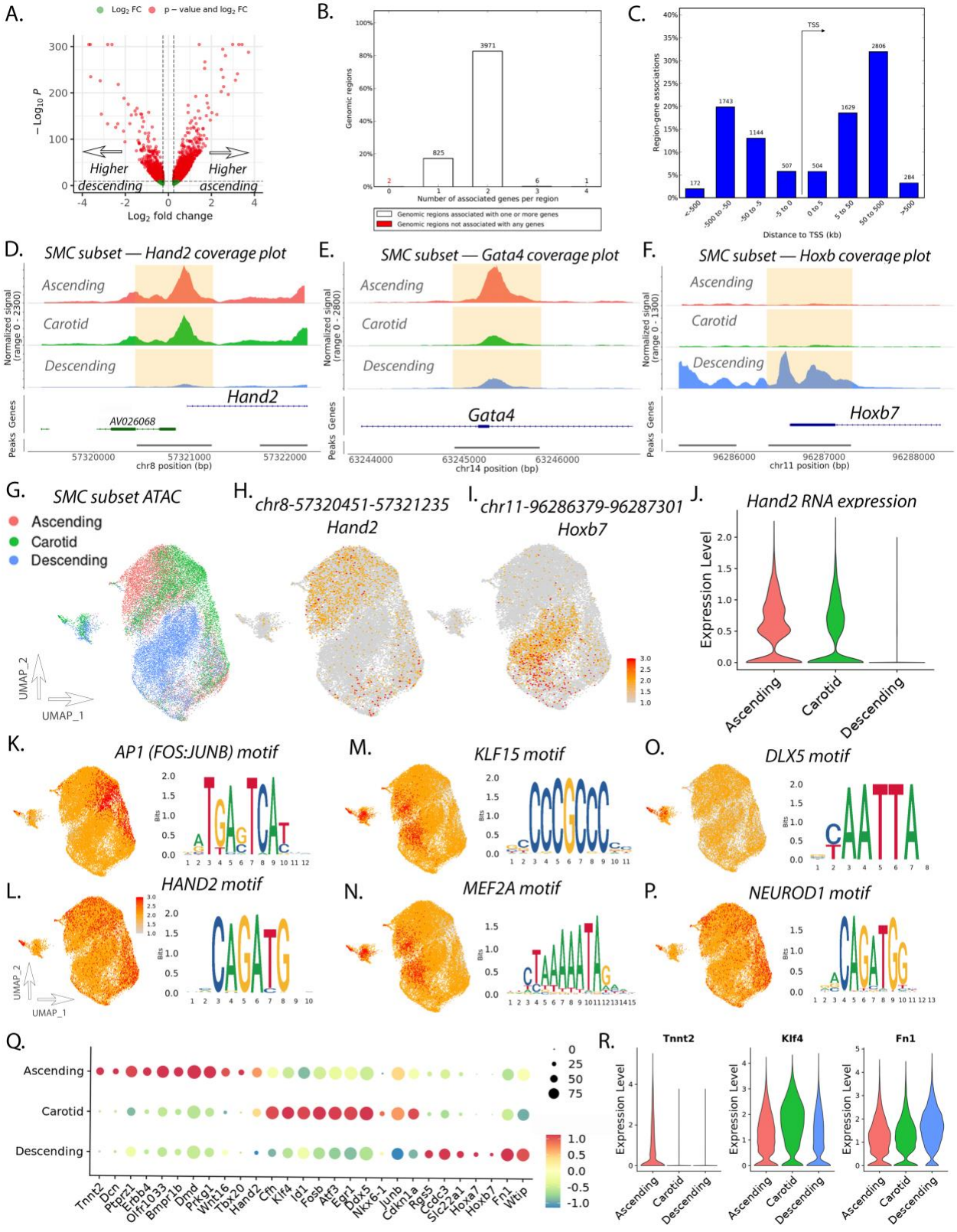
A.
Log2 FC
p – value and log2 FC
−Log10 P
Higher descending
Higher ascending
Log2 fold change
B.
Genomic regions
Number of associated genes per region
Genomic regions associated with one or more genes
Genomic regions not associated with any genes
C.
TSS
Region-gene associations
Distance to TSS (kb)
D.
SMC subset — Hand2 coverage plot
Ascending
Carotid
Descending
Normalized signal (range 0 - 2300)
Hand2
AV026068
Peaks Genes
chr8 position (bp)
E.
SMC subset — Gata4 coverage plot
Normalized signal (range 0 - 2800)
Gata4
chr14 position (bp)
F.
SMC subset — Hoxb coverage plot
Normalized signal (range 0 - 1300)
Hoxb7
chr11 position (bp)
G.
SMC subset ATAC
Ascending
Carotid
Descending
UMAP_1
UMAP_2
H.
chr8-57320451-57321235
Hand2
I.
chr11-96286379-96287301
Hoxb7
J.
Hand2 RNA expression
Expression Level
Ascending
Carotid
Descending
K.
AP1 (FOS:JUNB) motif
M.
KLF15 motif
O.
DLX5 motif
L.
HAND2 motif
N.
MEF2A motif
P.
NEUROD1 motif
Q.
Ascending
Carotid
Descending
Tnnt2
Dcn
Ptprz1
Erfb4
Olfr1033
Bmpr1b
Dmd
Prkg1
Wnt16
Tbx20
Hand2
Cfh
Klf4
Id1
Fosb
Atf3
Egr1
Ddx5
Nkx6-1
Junb
Cdkn1a
Rgs5
Ccdc3
Slc22a1
Hoxa7
Hoxb7
Fn1
Wtip
R.
Tnnt2
Klf4
Fn1
Expression Level
Ascending
Carotid
Descending

1331

1332 **Figure 2. SMC subset analysis reveals differential chromatin peak accessibility,**
1333 **gene expression, and transcription factor motif accessibility between vascular**
1334 **sites.** Volcano plot of differentially accessible peaks comparing ascending and
1335 descending SMC (A). Peak to gene analysis revealing number of associated genes per
1336 genomic region (B). Histogram of distance from peak to associated gene TSSs (C).
1337 Coverage plots of *Hand2* (D), *Gata4* (E), and *Hoxb* (F) for ascending, carotid, and
1338 descending SMC. UMAP of scATACseq data for SMC subset (G). Featureplot of *Hand2*
1339 (H) and *Hoxb7* (I) peaks. Violin plot of *Hand2* RNA expression between vascular sites
1340 (J). Featureplot of motif accessibility and motif sequence for *AP1* (K), *Hand2* (L), *Klf15*
1341 (M), *Mef2a* (N), *Dlx5* (O), and *Neurod1* (P). Dotplot of RNA expression for top
1342 differentially expressed transcripts (Q). Violinplot of SMC RNA expression across
1343 vascular sites for *Tnnt2*, *Klf4*, and *Fn1* (R).
1344

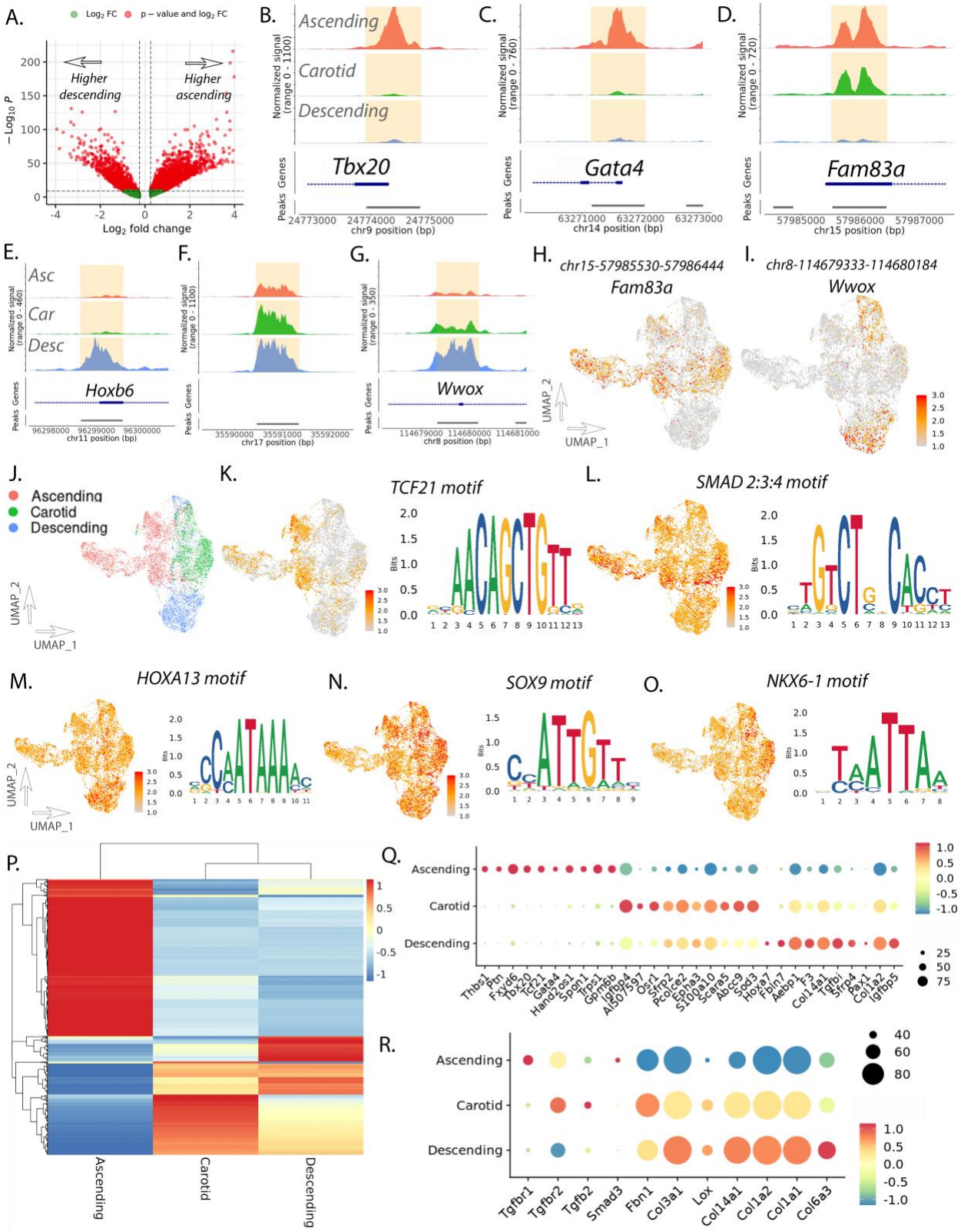
A.
Log2 FC
p – value and log2 FC
Higher descending
Higher ascending
−Log10 P
Log2 fold change
B.
Ascending
Carotid
Descending
Normalized signal (range 0 - 1100)
Tbx20
chr9 position (bp)
C.
Normalized signal (range 0 - 760)
Gata4
chr14 position (bp)
D.
Normalized signal (range 0 - 720)
Fam83a
chr15 position (bp)
E.
Asc
Car
Desc
Normalized signal (range 0 - 460)
Hoxb6
chr11 position (bp)
F.
Normalized signal (range 0 - 1100)
chr17 position (bp)
G.
Normalized signal (range 0 - 350)
Wwox
chr8 position (bp)
H.
chr15-57985530-57986444
Fam83a
UMAP_2
UMAP_1
I.
chr8-114679333-114680184
Wwox
J.
Ascending
Carotid
Descending
UMAP_2
UMAP_1
K.
TCF21 motif
L.
SMAD 2:3:4 motif
M.
HOXA13 motif
N.
SOX9 motif
O.
NKX6-1 motif
P.
Ascending
Carotid
Descending
Q.
Ascending
Carotid
Descending
Thbs1
Ptn
Fxyd6
Tbx20
Tcf21
Gata4
Hand2os1
Spon1
Trps1
Gpm6b
Igfbp4
Al507597
Osr1
Sfrp2
Pcolce2
Ephx3
S100a10
Scara5
Abcc9
Sod3
Hoxa7
Fbln7
Aebp1
F3
Col14a1
Tgfbi
Sfrp4
Pax1
Col1a2
Igfbp5
R.
Ascending
Carotid
Descending
Tgfbr1
Tgfbr2
Tgfb2
Smad3
Fbn1
Col3a1
Lox
Col14a1
Col1a2
Col1a1
Col6a3

1345

1346

1347 **Figure 3. Fibroblast subset analysis reveals vascular site-specific enhancers for**
1348 **developmental and disease genes.** Volcano plot of differentially accessible peaks
1349 between ascending and descending aortic fibroblasts (A). Coverage plot for ascending,
1350 carotid, and descending aortic fibroblasts at *Tbx20* (B), *Gata4* (C), *Fam83a* (D), *Hoxb6*
1351 (E), *chr17* gene desert (F), and *Wwox* (G). Featureplot of scATACseq data of fibroblast
1352 subset for peaks near *Fam83a* (H) and *Wwox* (I). UMAP of scATACseq data from
1353 fibroblast subset by vascular site (J). Featureplot of scATACseq for motif accessibility
1354 and motif sequence for *Tcf21* (K), *Smad2:3:4* (L), *Hoxa13* (M), *Sox9* (N), and *Nkx6-1*
1355 (O). Heatmap of scRNAseq differentially expressed genes in ascending, carotid, and
1356 descending fibroblast subset (P). Dotplot of scRNAseq transcript expression for top
1357 differentially expressed genes in fibroblast subset (Q). Dotplot of scRNAseq transcript
1358 expression for hereditary aortopathy genes (R).

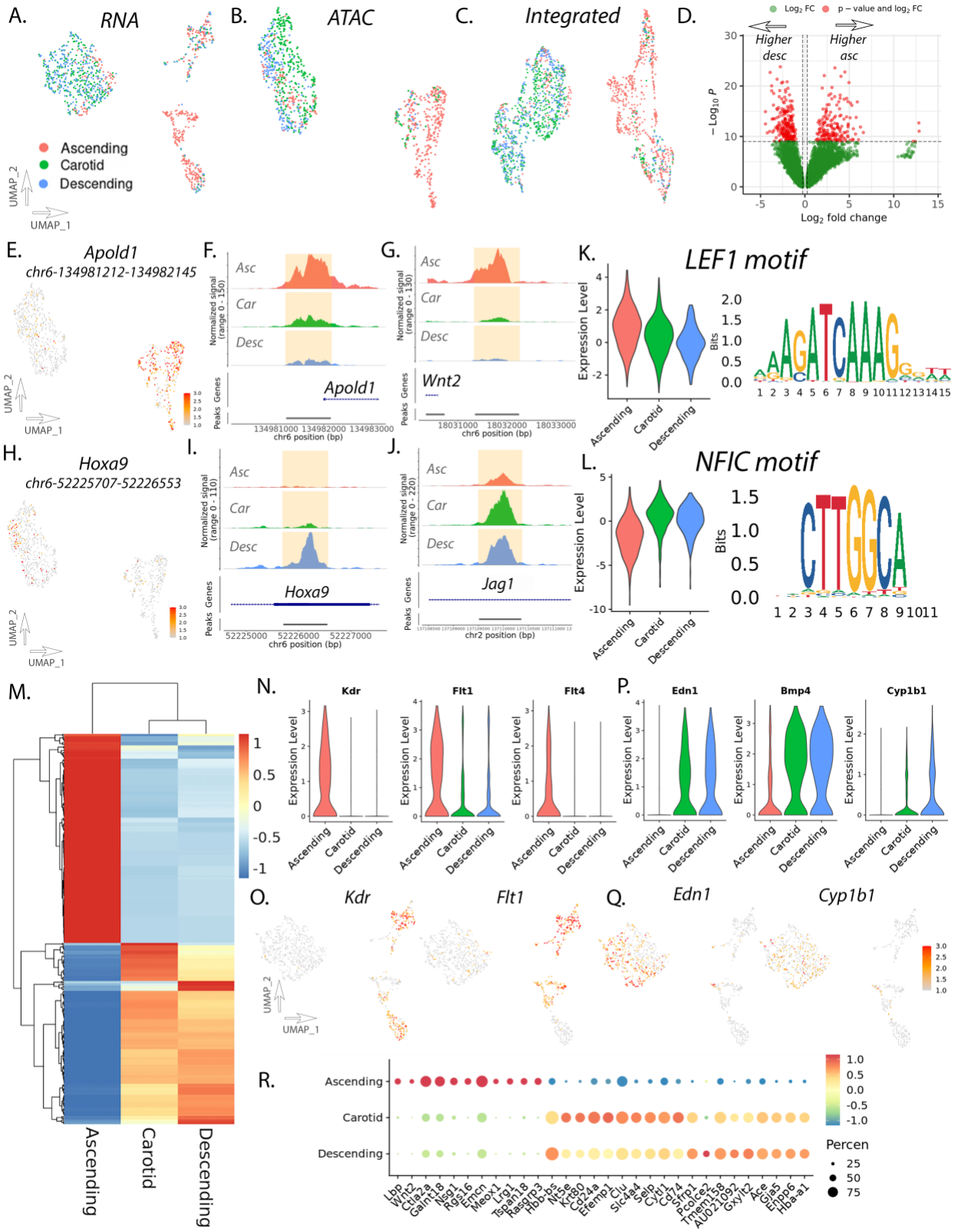
A.
RNA
B.
ATAC
C.
Integrated
D.
Ascending
Carotid
Descending
UMAP_2
UMAP_1
Log2 FC
p – value and log2 FC
Higher desc
Higher asc
−Log10 P
Log2 fold change
E.
Apold1
chr6-134981212-134982145
F.
G.
Asc
Car
Desc
Normalized signal (range 0 - 150)
Normalized signal (range 0 - 130)
Genes
Peaks
Apold1
Wnt2
chr6 position (bp)
K.
LEF1 motif
Expression Level
Ascending
Carotid
Descending
Bits
H.
Hoxa9
chr6-52225707-52226553
I.
J.
Normalized signal (range 0 - 110)
Normalized signal (range 0 - 220)
Hoxa9
Jag1
chr2 position (bp)
L.
NFIC motif
M.
N.
Kdr
Flt1
Flt4
P.
Edn1
Bmp4
Cyp1b1
O.
Q.
R.
Percen
25
50
75

1359

1360 **Figure 4. Endothelial cell subset analysis identifies differentially accessible**
1361 **chromatin peaks and differential transcription factor (TF) motif accessibility.**
1362 UMAP of RNA (A), ATAC (B), and integrated (C) datasets for endothelial cell subset.
1363 Volcano plot of differentially accessible peaks between ascending and descending
1364 endothelial cells (D). Featureplot of peak accessibility of *Apold1* peak (E). Coverage
1365 plots for *Apold1* (F) and *Wnt2* (G) genomic regions in endothelial cell subset.
1366 Featureplot of peak accessibility of *Hoxa9* peak (H). Coverage plots for *Hoxa9* (I) and
1367 *Jag1* (J) genomic regions in endothelial cell subset. Violinplot of motif accessibility and
1368 motif sequence for *LEF1* (K) and *NFIC* (L). Heatmap of differential RNA expression by
1369 endothelial cell vascular site (M). Violinplots of RNA expression in endothelial cells for
1370 *Kdr*, *Flt1*, and *Flt4* (N). Featureplots of RNA expression for *Kdr* and *Flt1* (O). Violinplots
1371 of RNA expression in endothelial cells for *Edn1*, *Bmp4*, and *Cyp1b1* (P). Featureplots of
1372 RNA expression for *End1* and *Cyp1b1* (Q). Dotplot of scRNAseq transcript expression
1373 for top differentially expressed genes in endothelial cell subset (R).

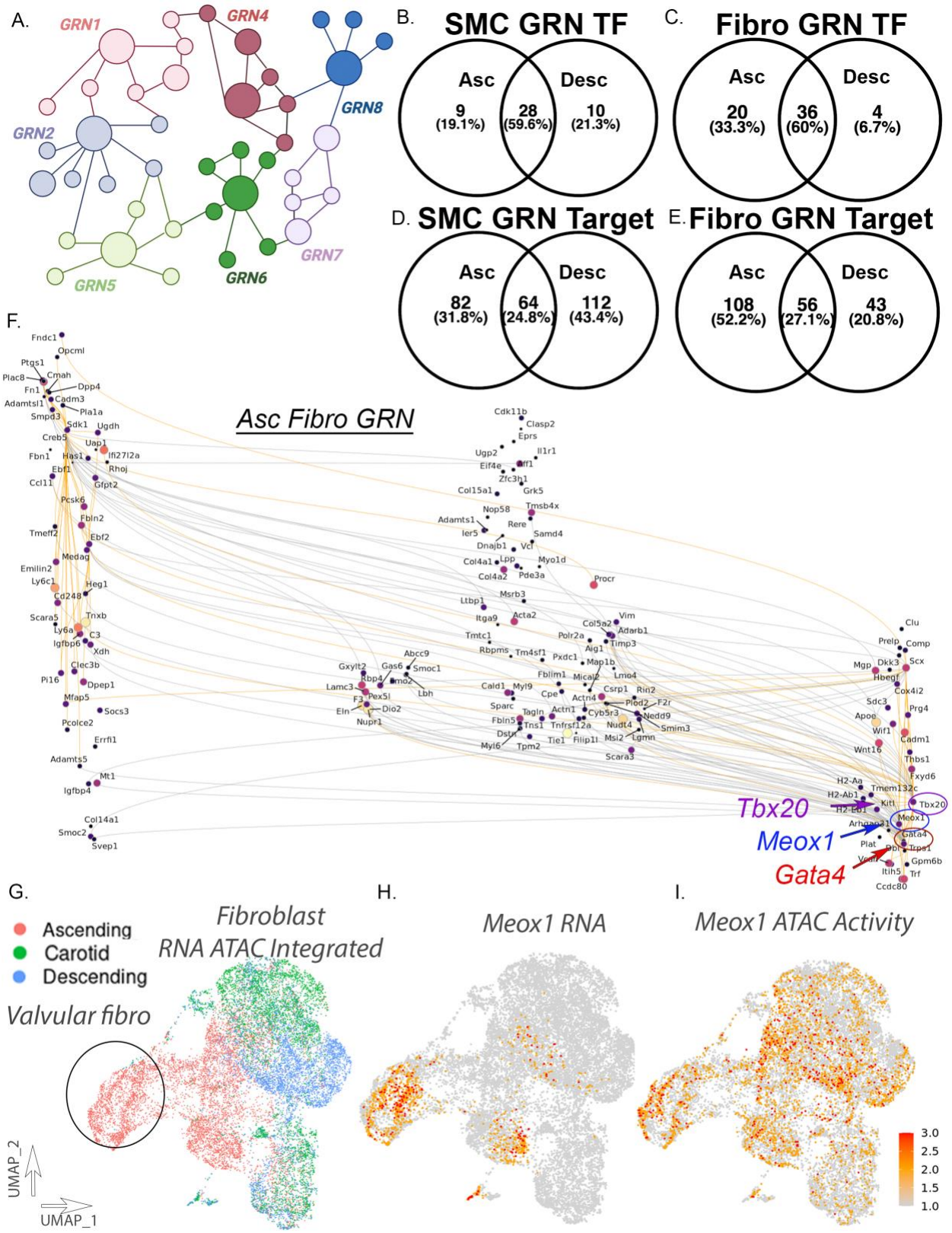
A.
GRN1
GRN2
GRN4
GRN5
GRN6
GRN7
GRN8
B.
SMC GRN TF
Asc
Desc
9 (19.1%)
28 (59.6%)
10 (21.3%)
C.
Fibro GRN TF
Asc
Desc
20 (33.3%)
36 (60%)
4 (6.7%)
D.
SMC GRN Target
Asc
Desc
82 (31.8%)
64 (24.8%)
112 (43.4%)
E.
Fibro GRN Target
Asc
Desc
108 (52.2%)
56 (27.1%)
43 (20.8%)
F.
Asc Fibro GRN
Tbx20
Meox1
Gata4
G.
Ascending
Carotid
Descending
Fibroblast
RNA ATAC Integrated
Valvular fibro
UMAP_2
UMAP_1
H.
Meox1 RNA
I.
Meox1 ATAC Activity
3.0
2.5
2.0
1.5
1.0

1374

1375 **Figure 5. Gene regulatory network analysis reveals cell type and vascular site-**
1376 **specific regulatory networks within the vessel wall.** Schematic diagram of gene
1377 regulatory networks (GRN)(A). Venn diagrams of GRN transcription factors comparing
1378 ascending and descending SMCs (B) and fibroblasts (C). Venn diagrams of GRN
1379 transcription factors gene targets comparing ascending and descending SMCs (D) and
1380 fibroblasts (E). GRN visualization for ascending fibroblasts network analysis (F). UMAP
1381 of scRNA/scATAC integrated fibroblast dataset by vascular site (G). Featureplot of
1382 *Meox1* RNA expression (H) and chromatin accessibility (I) in integrated fibroblast
1383 dataset.
1384
1385

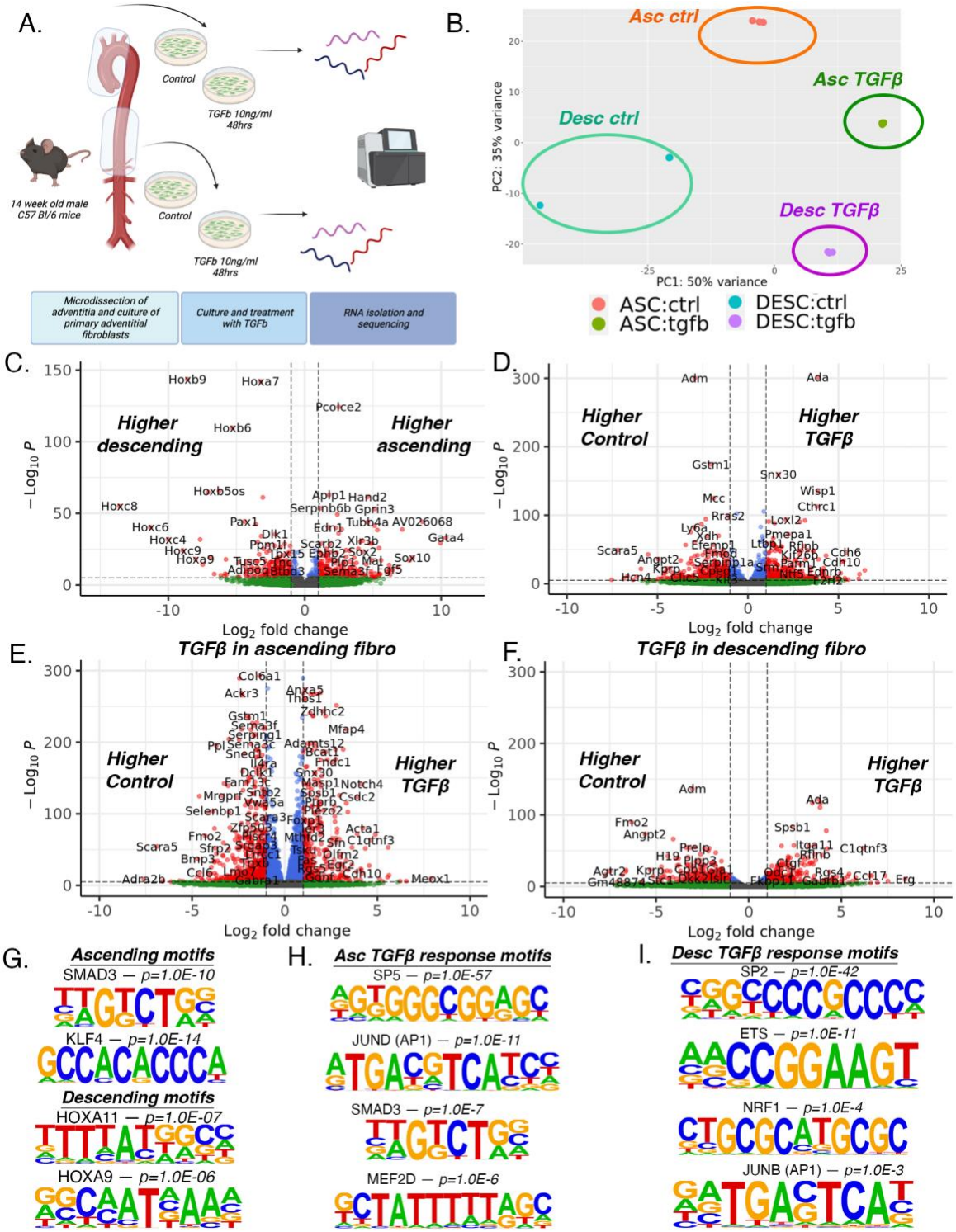

Figure 6. Primary adventitial fibroblasts retain vascular site-specific transcriptomic features following *in vitro* culture revealing vascular site-specific response to TGFβ. Schematic diagram of primary adventitial fibroblast culture,

1390 treatment, and bulk RNA sequencing (A). Principal component analysis (PCA) by
1391 vascular site and TGFβ treatment (B). Volcano plots showing differential gene
1392 expression analysis of all samples by vascular site (C) and by TGFβ treatment (D).
1393 Volcano plot of DE gene analysis in response to TGFβ in ascending (E) and descending
1394 (F) fibroblasts. Motif sequences of identified enriched transcription factors of 200bp
1395 sequences upstream of gene TSSs with increased expression in ascending and
1396 descending fibroblasts (G). Motif sequences of identified enriched transcription factors
1397 of 200bp sequences upstream of gene TSSs in of upregulated genes in ascending
1398 fibroblasts in response to TGFβ treatment (H) and descending fibroblasts in response to
1399 TGFβ treatment (I).
1400

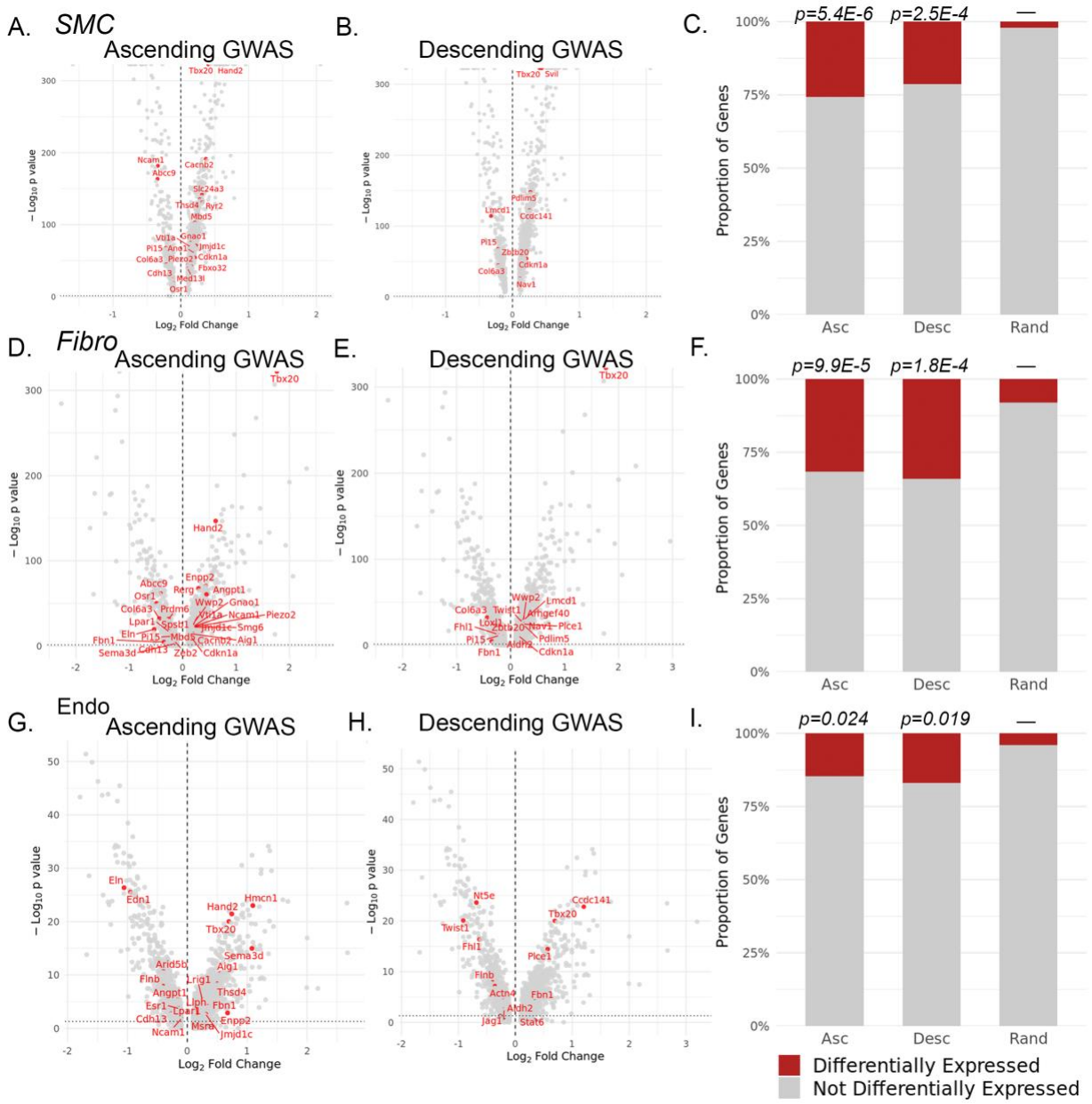

Figure 7. Aortic dimension GWAS genes are differentially expressed in a cell type and vascular site specific context. Volcano plots of ascending versus descending differential RNA expression and highlighting ascending and descending aortic dimension GWAS genes in SMC (A-B), fibroblast (D-E), and endothelial cells (G-H). Stacked barcharts showing the proportion of ascending/descending aortic dimension GWAS genes differentially expressed compared to random gene list in SMCs (C),

1408 fibroblasts (F), and endothelial cells (I). P values represent chi-quared statistical test for

1409 significance compared to random 100 gene list.

1410

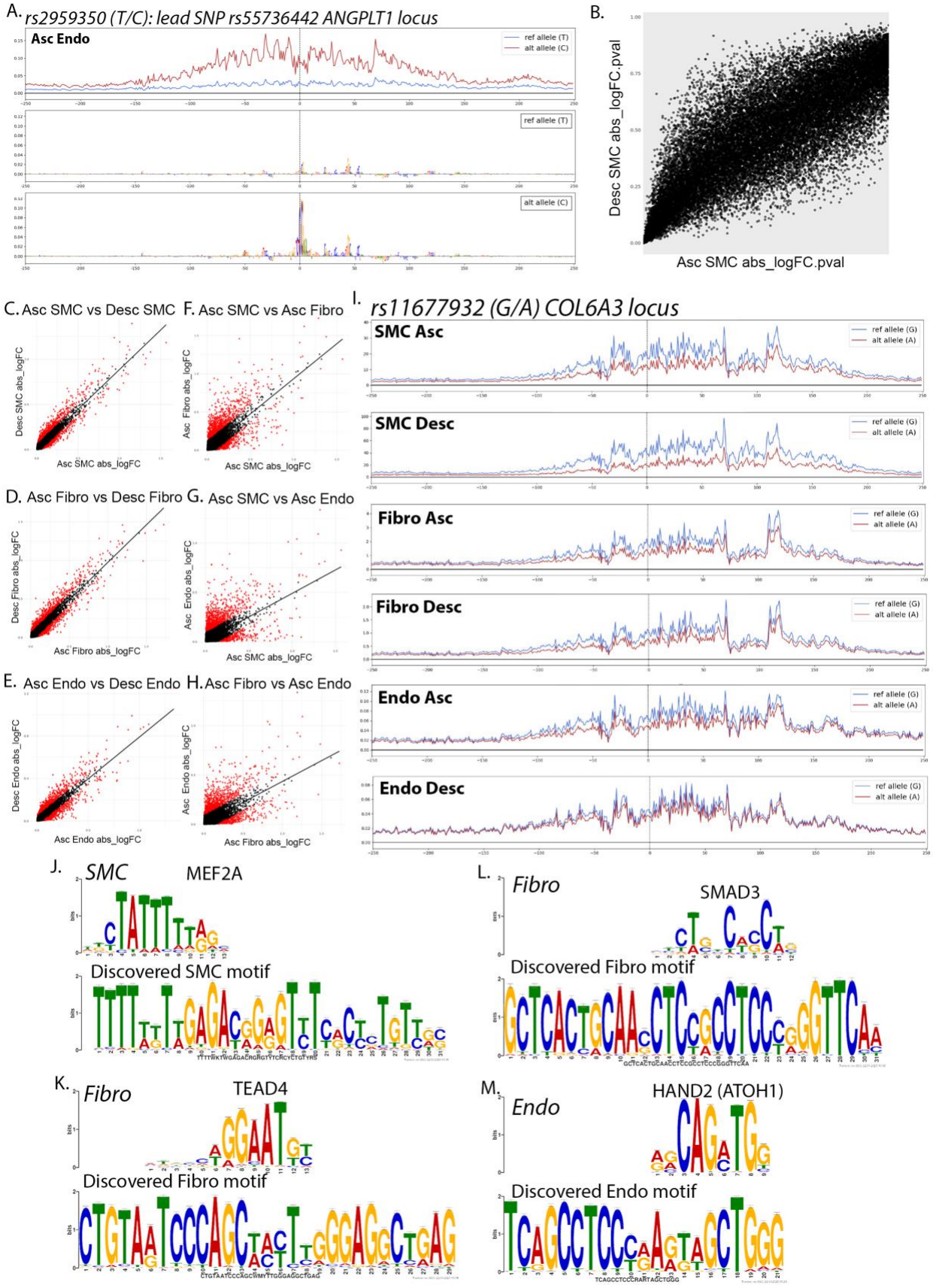
A. rs2959350 (T/C): lead SNP rs55736442 ANGPLT1 locus
Asc Endo
ref allele (T)
alt allele (C)
B.
Desc SMC abs_logFC.pval
Asc SMC abs_logFC.pval
C. Asc SMC vs Desc SMC
F. Asc SMC vs Asc Fibro
D. Asc Fibro vs Desc Fibro
G. Asc SMC vs Asc Endo
E. Asc Endo vs Desc Endo
H. Asc Fibro vs Asc Endo
Desc SMC abs_logFC
Asc SMC abs_logFC
Asc Fibro abs_logFC
Desc Fibro abs_logFC
Asc Endo abs_logFC
Desc Endo abs_logFC
I. rs11677932 (G/A) COL6A3 locus
SMC Asc
SMC Desc
Fibro Asc
Fibro Desc
Endo Asc
Endo Desc
ref allele (G)
alt allele (A)
J. SMC
MEF2A
Discovered SMC motif
L. Fibro
SMAD3
Discovered Fibro motif
K. Fibro
TEAD4
Discovered Fibro motif
M. Endo
HAND2 (ATOH1)
Discovered Endo motif

1411

1412 **Figure 8. ChromBPNet machine learning models predict variant effect on**
1413 **chromatin accessibility to be cell type and vascular site-specific.** Example locus of
1414 ChromBPNet prediction of chromatin accessibility in reference and alternative alleles for
1415 rs2959350 at *ANGPLT3* locus with predicted base pair contributing effects (A). Scatter
1416 plot of absolute log fold change (abs_logFC) p values for scored variants in ascending
1417 SMC versus descending SMC models (B). Scatter plots of abs_logFC for scored
1418 variants in ascending SMC versus descending SMC models (C), ascending fibro versus
1419 descending fibro models (D), ascending endothelial versus descending endothelial
1420 models (E), ascending SMC versus ascending fibroblast models (F), ascending SMC
1421 versus ascending endothelial models (G), and ascending fibroblast versus ascending
1422 endothelial models (H). Example locus of ChromBPNet prediction of chromatin
1423 accessibility in reference and alternative alleles for rs11677932 at *COL6A3* locus for
1424 ascending and descending SMCs, fibroblasts, and endothelial cell models (I). Examples
1425 of discovered and matched motifs in SMC – *MEF2A* (J), Fibroblasts – *TEAD4* (K),
1426 Fibroblasts – *SMAD3* (L), and Endothelial – *HAND2* (M).
1427
1428
1429